Journal of Alloys and Compounds 948 (2023) 169593

Contents lists available at ScienceDirect

Journal of Alloys and Compounds

journal homepage: www.elsevier.com/locate/jalcom

3D $Ti_3C_2T_X$@PANI-reduced graphene oxide hydrogel and defective reduced graphene oxide hydrogel as anode and cathode for high-energy asymmetric supercapacitor

Peng Liao [a,b], Yang Zeng [a], Zenghui Qiu [a,b,**], Shengcai Hao [c], Jiaqi He [a,*], Haijun Xu [a,b,**], Shaowei Chen [d,*]

[a] College of Mathematics and Physics, Beijing University of Chemical Technology, Beijing 100029, China
[b] Beijing Bioprocess Key Laboratory, Beijing University of Chemical Technology, Beijing 100029, China
[c] Beijing Institute of Electro-machining Co., Ltd., Beijing Key Laboratory of Electro Discharge Machining Technology, Beijing 100191, China
[d] Department of Chemistry and Biochemistry, University of California, 1156 High Street, Santa Cruz, CA 95064, United States

ARTICLE INFO

Article history:
Received 4 January 2023
Received in revised form 6 March 2023
Accepted 7 March 2023
Available online 10 March 2023

Keywords:
$Ti_3C_2T_X$ @PANI heterostructure
Intercalation process
Defective reduced graphene oxide
3D porous hydrogel
High performance
Asymmetric supercapacitors

ABSTRACT

The rational constructions of asymmetric supercapacitors (ASCs) by extending the operating potential window has been verified as an effective tactic to break through the energy density of the device. In this work, $Ti_3C_2T_X$ @polyaniline (PANI) heterostructure is successfully synthesized by uniformly depositing PANI nanorods onto the surface of $Ti_3C_2T_X$ nanosheets through polymer polymerization, then via a low-temperature hydrothermal graphene oxide (GO)-gelation process, $Ti_3C_2T_X$ @PANI is assembled into a three-dimensional (3D) porous hydrogel. The resultant $Ti_3C_2T_X$ @PANI-reduced graphene oxide (RGO) hydrogel exhibits a high specific capacitance of 617.84 F g^{-1} at 0.5 A g^{-1}. Separately, a defective reduced graphene oxide (DRGO) hydrogel is prepared by a cost-effective cobalt-catalyzed gasification procedure, which shows a higher specific capacitance (237.62 F g^{-1} at 0.5 A g^{-1}) than that of untreated RGO hydrogel (158 F g^{-1}). Finally, $Ti_3C_2T_X$ @PANI-RGO and DRGO are used as anode and cathode to construct the $Ti_3C_2T_X$ @PANI-RGO// DRGO ASC device, which features a stable operating voltage (−1.6 to 0.2 V), an ultra-high energy density (269.18 Wh kg^{-1} at 527.72 W kg^{-1} and 77.90 Wh kg^{-1} at 12,409.04 W kg^{-1}), and durable cycling property (retaining 92.52% capacitance after 10,000 cycles at 10 A g^{-1}). This research emphasizes the extraordinary superiority of $Ti_3C_2T_X$-based structures for the construction of high-energy ASCs.

1. Introduction

Electrical energy can be stored in two different ways: one is indirect, where potentially usable chemical energy is stored in the battery by electrochemically active species undergoing a Faradaic redox reaction; second is the direct method, which is a non-Faraday energy storage process in which positive and negative charges are electrostatically stored between the different plates of the capacitor [1–3]. Since combustion systems are limited by the thermodynamic Carnot cycle, batteries and capacitors involve highly reversible processes that convert available chemical energy into free energy, resulting in more efficient electrical energy storage [4–6]. The difference between batteries and capacitors is that the electrodes of batteries usually undergo an inherent phase transition during charging and discharging, which causes the kinetics and thermodynamics of the reaction to be irreversible, whereas capacitors do not have substantial phase transitions [7,8]. Supercapacitors (SCs) are a fresh kind of energy storage installation that combines traditional capacitors with rechargeable batteries, can be categorized into electric double-layer capacitors (EDLCs), pseudocapacitors, and ASCs [9–12]. EDLCs store charge by enhancing the electrostatic process of positive and negative charges attracting each other, and no charge transfer occurs between electrode and electrolyte [13,14]. Pseudocapacitors store charge by the Faraday process, which involves charge transfer between electrode and electrolyte [15–17]. ASCs refer to devices based on battery-type anode and capacitive-type cathode [18–21].

* Corresponding authors.
** Corresponding authors at: College of Mathematics and Physics, Beijing University of Chemical Technology, Beijing 100029, China.
E-mail addresses: zhqiu@buct.edu.cn (Z. Qiu), jqhe@buct.edu.cn (J. He), hjxu@buct.edu.cn (H. Xu), shaowei@ucsc.edu (S. Chen).

https://doi.org/10.1016/j.jallcom.2023.169593
0925-8388/

The two-dimensional (2D) nanomaterials refer to crystalline materials with a thickness of single or multiple atomic layers, whose inherent high specific surface area can provide high electric double-layer capacitance and huge reaction planes, and corners can provide pseudocapacitance [22–24]. In addition, 2D nanomaterials can also provide additional reaction sites through loading or surface functional group modification to enhance specific capacity, while 2D channels between their sheets can provide rapid ion diffusion rates [25–27]. Therefore, 2D nanomaterials have aroused great attention in electrochemical energy storage as supercapacitor electrodes [28,29]. MXenes are typical 2D nanomaterials, which are also 2D transition-metal carbides/nitrides/carbonitrides with the general formula $M_{n+1}X_nT_Z$, where M is a transition metal (Sc, Ti, V, Cr, Zr, Nb, Mo, Hf, or Ta), X is carbon and/or nitrogen, n is generally 1–3, and T_Z is a surface functional group [30–32]. 2D accordion-structured materials, MXenes, are usually synthesized by a strategy of corroding the "A" element from the MAX precursor [33–35]. Up to this point, among the successful prepared MXenes family, $Ti_3C_2T_X$ is the most deeply researched and most applied widely [36].

However, because of the van der Waals powers, the interlayer structures of $Ti_3C_2T_X$ will attract each other, resulting in the stacking of interlayer structures and reduced specific surface area, which seriously affects their electrochemical performance [37,38]. In order to overcome agglomeration, the strategy of synthesizing $Ti_3C_2T_X$ @ PANI heterostructures by inserting PANI into the interlayer structure of $Ti_3C_2T_X$ can open the interlayer separating to augment the particular surface region [39–42]. PANI is a polymer capacitor electrode material with various structures, good chemical stability, high conductivity and large relative molecular mass, which is polymerized from Aniline (ANI) as a monomer [43,44]. Moreover, PANI is also a typical π-π conjugated conductive polymer, and its main chain contains repeating units of alternating single and double bonds, and this molecular structure arrangement can delocalize the antibonding molecular orbitals of the molecular main chain [45,46]. Under the influence of an electric field, PANI undergoes a redox reaction which is a rapid, reversible doping and dedoping process of p-type and n-type elements, during which a large amount of charge is stored [47,48]. GO is a sheet-like structure composed of single-atom-thick hexagonal units, which is composed of phenolic hydroxyl and epoxy functional groups located on the upper and lower surfaces of the sheet, and carboxyl and carbonyl groups containing sp^2 hybridized carbons mainly at the edge of the sheet [49–52]. Besides, the $Ti_3C_2T_X$ @PANI-RGO hydrogel with a 3D porous structure was hydrothermally assembled at low temperature [53,54]. Obviously, the $Ti_3C_2T_X$ @PANI-RGO hydrogel is a suitable anode material for ASCs with remarkable pseudocapacitive property [55–58].

It is well known that due to the interlayer π-π bonds, the RGO obtained from chemical reduction of GO will undergo severe aggregation, resulting in the narrowing of ion transport channels and destroying the capacitive properties [59]. Through defect engineering with widely distributed mesopores in the surface structure of RGO, the aggregation of RGO can be suppressed, which provides abundant pathways for ion penetration to improve the specific capacitance [60,61]. There are three main types of defects in graphene: vacancy defects, surface adsorption impurities and topological defects [62]. And 3D DRGO can be prepared by a strategy of using Co particles to catalyze C atoms in contact with the RGO surface to create defects followed by acid wash etching [63]. Obviously, DRGO hydrogel has remarkable electric double-layer capacitance and is a typical ASC negative electrode material [64–67].

In this work, 3D $Ti_3C_2T_X$ @PANI-RGO hydrogels were fabricated by an efficient method and used as positive electrode for ASCs. This $Ti_3C_2T_X$ @PANI heterostructures synthesized by chemisorption and polymer polymerization process are then assembled into a 3D porous cross-linked hydrogel by a GO-assisted self-converging process. DRGO hydrogels are synthesized by a Co-catalyzed gasification method, which is acted as a negative electrode. The $Ti_3C_2T_X$ @PANI-RGO//DRGO ASC device is constructed, and features an expanded voltage window of 1.8 V, a maximum energy density of 269.18 Wh kg^{-1} at 527.72 W kg^{-1} and outstanding reversibility (92.52% capacitance retention over 10,000 cycles).

2. Experimental section

2.1. Material preparation

2.1.1. $Ti_3C_2T_X$ MXene

The layered $Ti_3C_2T_X$ MXenes were synthesized by purposely corroding the Al thickness of the Ti_3AlC_2 precursor (< 38 μm, 98%) [68]. Firstly, dissolve 1 g of LiF (99%) in 20 mL of 9 M HCl (36%) aqueous solution, and stir in an ice bath for 1 h and slowly add 1 g of Ti_3AlC_2 powder [69]. Subsequently, the mixture by persistent magnetic stirring was reacted at 45 °C for 48 h to etch the Al layer. Then, the $Ti_3C_2T_X$ suspension was cleaned 6 times with deionized water and absolute ethanol by repeated centrifugation at 5000 rpm (10 min per cycle) until the pH reached about 7. The homogeneous disperse colloidal solutions of $Ti_3C_2T_X$ were prepared by sonicating and centrifuging (5000 rpm) the above product for 2 h under Ar gas flow. Finally, $Ti_3C_2T_X$ was obtained by collecting the supernatant and freeze-dried.

2.1.2. $Ti_3C_2T_X$ @PANI heterostructure

Firstly, 0.2 g $Ti_3C_2T_X$ MXenes were dissolved in 50 mL 2 M HCl aqueous solution [70]. Then, after adding 100 mL of ANI (99.5%) to the above solution, magnetic stirred at 5 °C for 30 min[71] Subsequently, 20 mL of 2 M HCl aqueous solution dissolved with 0.335 g of ammonium persulfate (APS, 98.0%) was appended to the above hybrid, and it was magnetic stirred at 5 °C for 7 h. The above product was sonicated for 1 h and washed several times by centrifugation (5000 rpm) in deionized water and absolute ethanol. Finally, clean $Ti_3C_2T_X$ @PANI heterostructure was synthesized by lyophilization for 48 h [72]. PANI was synthesized in the identical way without the addition of $Ti_3C_2T_X$ [73].

2.1.3. 3D $Ti_3C_2T_X$ @PANI-RGO hydrogel

The synthesis of 3D $Ti_3C_2T_X$ @PANI-RGO hydrogel was performed by using a GO-assisted self-convergence strategy at low temperature. GO was fabricated from natural graphite flakes (90%) by an improved Hummers' method [74]. A GO homogeneous colloidal suspension (2 mg mL^{-1}) was prepared by ultrasonication of GO in deionized water for 6 h, followed by centrifugation (3800 rpm for 1 h) to remove thick layers. Then, the $Ti_3C_2T_X$ @PANI heterostructure particles (8 mg) were dispersed in 2 mL of the gained GO colloid solution followed by magnetic stirring for 1 h, and then 8 mg of Vitamin C (GO/Vitamin C mass ratio 1:2) was appended for sonication for 2 h. After hydrothermal process at 90 °C for 6 h, $Ti_3C_2T_X$ @ PANI-RGO hydrogel was generated, washed with deionized water and ethanol for 5–6 times until pH was about 7. For comparison, RGO hydrogel and $Ti_3C_2T_X$-RGO were synthesized in the identical method without PANI [75].

2.1.4. Preparation of DRGO and RGO hydrogels

The homogeneous GO/Co (the mass ratio of GO/Co was 9:1) mixture dispersion was achieved by a strategy of vigorously stirring and sonicating for 2 h after diffusing 0.2 mg Co particles (99.9%) into 0.9 mL GO colloidal solution (2 mg mL^{-1}) [76]. The above mixture was added with 3.6 mg Vitamin C (the mass ratio of GO/Vitamin C is 1:2) with mechanical stirring for 30 min, and the resulting solution was heated at 90 °C for 6 h to obtain a RGO hydrogel with a homogeneous attachment of Co particles on the surface, and then oxidized in an air atmosphere of 350 °C for 0.5 h. The cobalt oxide was then removed by immersion in the seething concentrated nitric

acid solution for 1 h. Finally, the 3D DRGO hydrogels were cleaned with deionized water until the pH value is neutral. For comparison, RGO hydrogel was prepared in the same method but without Co particles.

2.2. Structural characterization

SEM images were tested with a scanning electron microscope (SEM, Zeiss, Gemini 300). Structure of the composite fibers was analyzed using transmission electron microscopy (TEM) (JEOL-2100, Japan) coupled with energy dispersive X-ray (EDX) spectroscopy and selective area electron diffraction (SAED). ImageJ software was used to determine the distance of the lattice fringes. X-ray diffraction (XRD) was performed using an X-ray diffractometer (Rigaku Ultima IV, λ = 0.15418 nm), Raman spectroscopy was performed by a Raman spectrometer (HORIBA Scientific LabRAM HR Evolution, laser excitation wavelength 532 nm), and X-ray photoelectron spectroscopy (XPS) was conducted by a XPS photoelectron spectrometer (Thermo Scientific K-Alpha). Thermal analysis (TGA) was measured by a thermogravimetric analyzer (TA TGA5500). The N_2 adsorption–desorption isotherms of all samples were evaluated using a nanometric analyzer (Nanoporosity-XQ, Korea). The specific surface areas were estimated using the Brunauer–Emmett–Teller (BET) model. The Barrett–Joyner–Halenda (BJH) model was performed to calculate the pore volume and pore size distribution.

2.3. Electrochemistry

Electrochemical tests were performed traditionally in a three-electrode system (working electrode, Ag/AgCl reference electrode, and Pt foil counter electrode) using a CHI 660B electrochemical workstation with 1 M KOH (85.0%) electrolyte. Active materials were vacuum-dried at 70 °C for 48 h and then soaked in 1 M KOH electrolyte for 36 h to accomplish electrolyte balance. Owing to good mechanical property, these as-prepared hydrogels can be used as electrodes without binder with the active material loading of about 1.0 mg. According to the GCD curves, the specific capacitance (C, F g^{-1}) can be calculated by the equation (1): $C = It/mU$, where I (A) is the electric current, t (s) is the discharge time, m (g) is the mass of the active material of the electrode and U (V) is the potential window.

2.4. ASC device

The free-standing $Ti_3C_2T_X$ @PANI-RGO//DRGO ASC device was constructed by using $Ti_3C_2T_X$ @PANI-RGO hydrogel as anode and DRGO hydrogel as cathode. The ASC device balances the relative masses of the anode and cathode through the conservation of positive and negative charges and is tested in a two-electrode framework. Considering the electrochemical reactions of the positive and negative electrodes at the same time can achieve the best performance, so the mass of the positive electrode needs to match the negative electrode to achieve charge conservation. And the calculation of the charge balance is calculated by the equation (2): $Q = CVm$; $Q_+ = Q_-$; $m_+/m_- = C_-V_-/C_+V_+$, where Q_+ and Q_- refer to the charge stored at the anode and cathode, C_+ and C_- is the specific capacitance of the anode and cathode in three-electrode system, V_+ and V_- represent the potential window, and m_+ and m_- stand for the active material mass in the anode and cathode, respectively.

3. Result and discussion

3.1. Structure and electrochemical characteristics of anode material

The layered $Ti_3C_2T_X$ @PANI heterostructures synthesis approach is depicted in Fig. 1a. First, the surface of $Ti_3C_2T_X$ nanosheets was uniformly decorated with organic ANI monomers via chemisorption. The ANI was then placed in an ice bath and polymerized via chemical oxidation with the help of an initiator. The reaction procedure can be divided into three stages, chain induction and initiation period, chain growth period and chain termination period. The dimer was formed in the first stage, and then the polymerization entered the second stage. The reaction began to accelerate itself, the precipitation appeared rapidly, and the system give out heat a lot, which was further accelerated to the third stage. Finally, ANI monomers were polymerized into PANI nanorods, and the $Ti_3C_2T_X$ @ PANI heterostructure could be obtained in acidic medium.

Fig. 1b displays that $Ti_3C_2T_X$ MXene has a 2D layered accordion structure, but due to the existence of molecular forces, the interlayer structures attract each other and lead to tight packing. From Fig. 1c, one can see that the main body of the synthesized PANI is in the shape of nanorods, and a small part is in the shape of nanosheets, which strongly verifies the reliability of the polymerization of ANI into PANI by chemical oxidation. Moreover, the PANI synthesized according to this strategy exhibits dark green color at the macroscopic level, which belongs to the PANI in the highly conductive state, and the electrochemical performance is obviously higher than that of the black eigenstate PANI. In Fig. 1d, dense PANI nanorods is grown on the interlayer structure of $Ti_3C_2T_X$, which significantly enlarges the interlayer spacing and expands the specific surface area. In Fig. 1e, the $Ti_3C_2T_X$ nanosheets exhibit a thin wrinkled 2D planar structure, while the structure in Fig. 1f has many larger granular structure, which is mainly from PANI nanorods. It is shown that the $Ti_3C_2T_X$ @PANI heterostructures have layered structures, and the surface and interlayer structures of $Ti_3C_2T_X$ are homogeneously deposited by dense nanorod-like PANI, manifesting that the components are tightly assembled together microscopically.

The HRTEM research is shown in Fig. 1g, a group of obvious lattice stripes with a lattice fringe spacing of 0.37 nm is displayed. Because PANI is not a crystal of strict standard, it is difficult to show lattice stripes. Therefore, it is obvious that this group of lattice stripes belongs to $Ti_3C_2T_X$ and is within the range of crystal plane spacing of $Ti_3C_2T_X$. The SAED pattern (Inset in Fig. 1g) reveals three strong rings attributing to 0.25, 0.15, and 0.13 nm crystal plane spacing, and can be separately signed with (111), (220), and (311) crystal planes. HRTEM and SAED analysis results are conformed with $Ti_3C_2T_X$, which further confirms the successful preparation of $Ti_3C_2T_X$. Fig. 1a-g show the layering $Ti_3C_2T_X$ @PANI heterostructures have close aspectant contact between $Ti_3C_2T_X$ and PANI, which can supply rich channels for ion transport, as well as provide stable mechanical property, thus producing good electrochemical performance. More structural details of the heterostructure were gained by EDX analysis. C, N, O, and Ti elements contained in $Ti_3C_2T_X$ @PANI heterostructures were easily identified (Fig. S1a, Supporting Information), and the characteristic N element mainly derived from PANI accounted for 3.65% (Fig. S1a inset, Supporting Information). It can be seen from the corresponding element distribution diagram (Fig. S1b, Supporting Information) where these components are evenly distributed in the heterostructure, which confirms the efficient combination of PANI nanorods and $Ti_3C_2T_X$ nanosheets.

The crystal phases and molecular structures of the $Ti_3C_2T_X$, PANI, and $Ti_3C_2T_X$ @PANI were investigated using XRD pattern and Raman spectroscopy. Fig. 2a displays that the XRD spectra of $Ti_3C_2T_X$, PANI, and $Ti_3C_2T_X$ @PANI. The strong peaks at 18°, 30.2°, 35.9°, 60.5°, and 72.3° in the $Ti_3C_2T_X$ @PANI heterostructure (blue curve) are derived from (111), (220), (111), and (311) lattice of $Ti_3C_2T_X$ (red curve, JCPDS 71–0298). And characteristic peaks corresponding to PANI (green curve) about at 15.3°, 19.2°, 25.4°, and 29.1° can be seen in the curve of the $Ti_3C_2T_X$ @PANI. In addition, in the heterostructure, the characteristic diffraction peak corresponding to $Ti_3C_2T_X$ at 30.2° and 35.9° broadens and moves to a lower angle, which indicates that the insertion of PANI nanorods into $Ti_3C_2T_X$ nanosheets broadens the

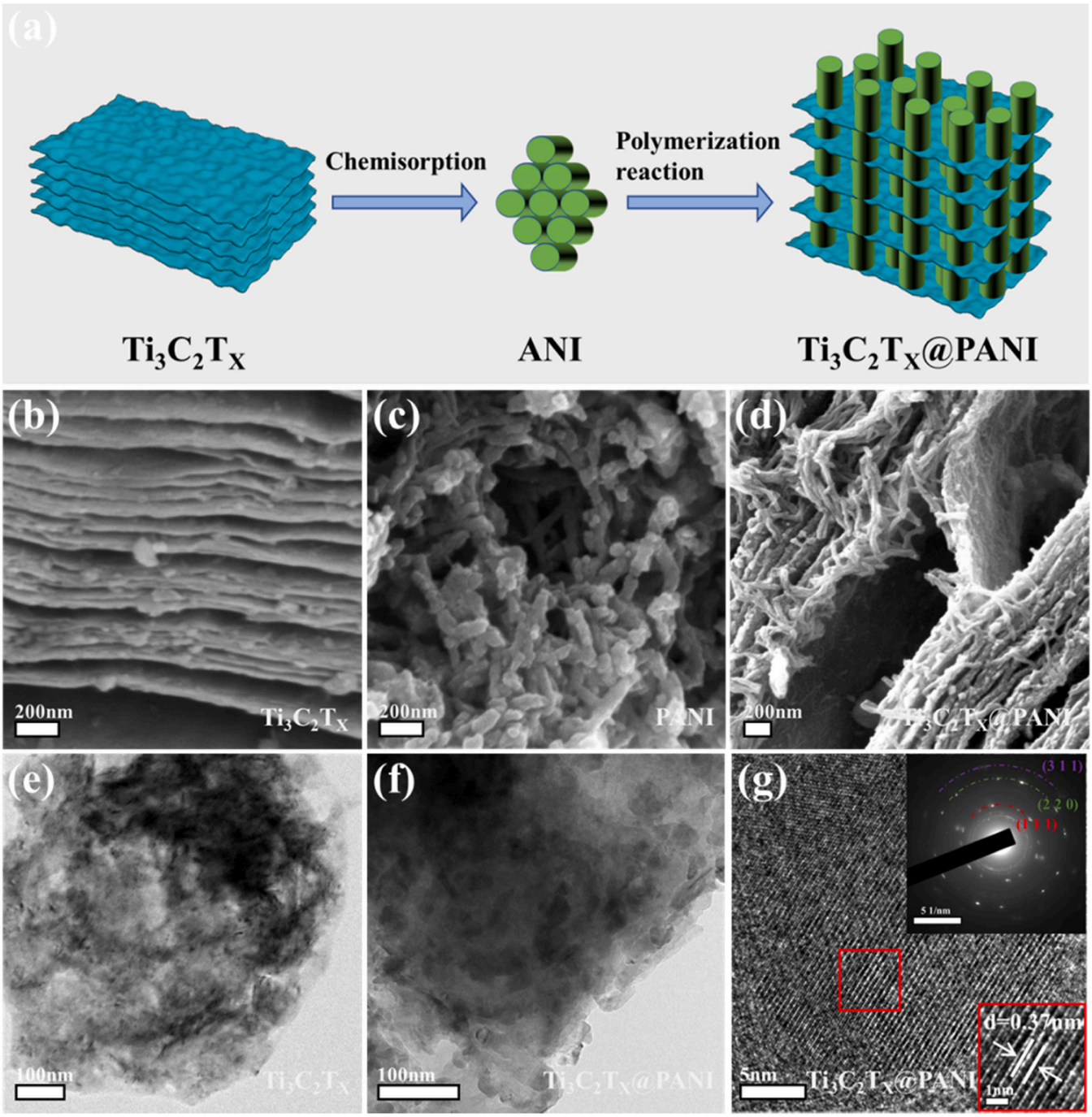

Fig. 1. (a) Schematic diagram of the synthesis process of $Ti_3C_2T_X$ @PANI. SEM images of (b) $Ti_3C_2T_X$, (c) PANI, and (d) $Ti_3C_2T_X$ @PANI. TEM images of (e) $Ti_3C_2T_X$, (f) $Ti_3C_2T_X$ @PANI. (g) HRTEM image of $Ti_3C_2T_X$ @PANI, with corresponding SAED pattern is in the inset.

interlayer spacing of $Ti_3C_2T_X$, and effectively inhibiting the dense stacking of $Ti_3C_2T_X$. According to the Raman spectrum in Fig. 2b, Raman peaks of $Ti_3C_2T_X$ (red curve) and $Ti_3C_2T_X$ @PANI (Blue curve) located in 283, 423, and 614 cm^{-1}, attributing to Ti-C vibrating key. At the same time, the Raman spectrum of PANI (green curve) and $Ti_3C_2T_X$ @PANI (Blue curve) heterostructures show characteristic peaks at 1180, 1338, and 1495 cm^{-1}, respectively, attributing to C-H bending of quinoid ring, C-N stretching of benzenoid and C-N stretching of quinoid. Furthermore, no additional peaks were detected, which further confirmed that PANI nanorods were homogeneously deposited on the entire surface of $Ti_3C_2T_X$.

The elemental compositions and chemical bonding states of the samples were analyzed by XPS spectra. From Fig. 2c and d, we can see that the photoelectron lines located at about 284, 399, 459, and 530 eV of the layered $Ti_3C_2T_X$ nanosheets and $Ti_3C_2T_X$ @PANI heterostructure can be separately caused by C, N, Ti, and O elements. Moreover, it can be detected that after PANI was deposited on the outside of $Ti_3C_2T_X$ nanosheets, the intensity of characteristic peak corresponding to N 1 s increased significantly. Since the N element is mainly derived from the conducting polymer PANI, this strongly indicates that there are obviously PANI nanorods in the $Ti_3C_2T_X$ @ PANI heterostructure samples.

Fig. 2e-h show the corresponding elemental spectra of $Ti_3C_2T_X$ @ PANI heterostructure. In Fig. 2e, the C 1 s electron can be scanned with high resolution to find four peaks at 283, 284.4, 285.9, and 288.1 eV, respectively attributing to C-Ti, C-C, C-N, and C=O. In the N

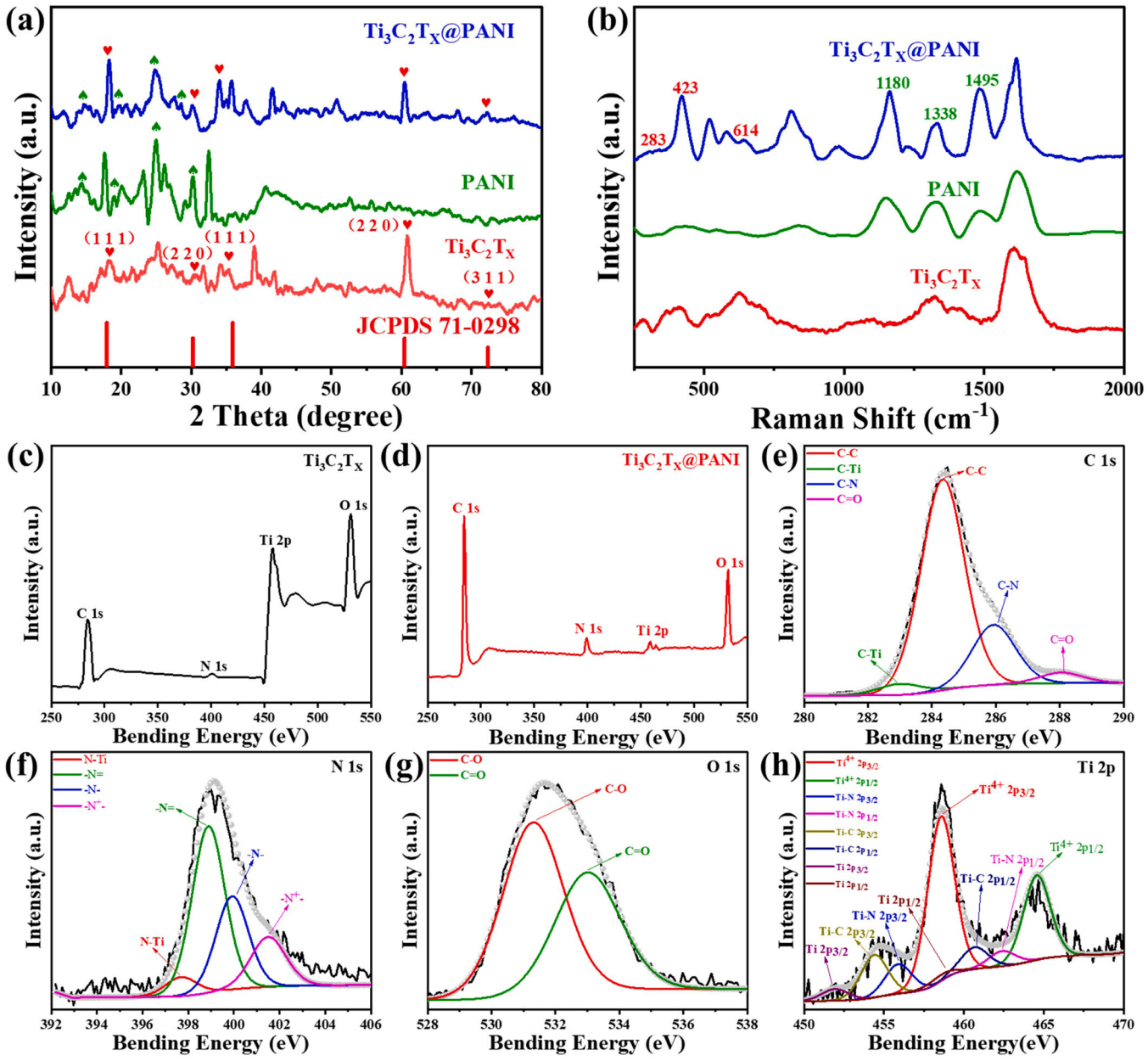

Fig. 2. (a) XRD patterns and (b) Raman scattering spectra of $Ti_3C_2T_X$, PANI, and $Ti_3C_2T_X$ @PANI heterostructure. XPS spectra of (c) $Ti_3C_2T_X$ and (d) $Ti_3C_2T_X$ @PANI heterostructure. High-resolution spectra of $Ti_3C_2T_X$ @PANI heterostructure: (e) C 1 s, (f) N 1 s, (g) O 1 s, and (h) Ti 2p electrons.

1 s spectrum (Fig. 2f), N-Ti, -N = , -NH-, and $-N^+$- are located at 398.1, 398.9, 399.9, and 401.5 eV, respectively. Moreover, the peaks of N-Ti, -N = , -NH-, and $-N^+$- are mainly from the PANI produced by the polymerization of ANI monomers containing amino groups, indicating the successful occurrence of polymer polymerization. The adsorption process of microscopic electron transfer, exchange and sharing between adsorbate and adsorbent is called chemisorption, which is characterized by the formation of new adsorption chemical bonds. Since C and Ti elements come from $Ti_3C_2T_X$ nanosheets, and N elements come from PANI nanorods, the occurrence of peaks of C-N bond (Fig. 2e) and N-Ti bond (Fig. 2f) not only proves that PANI nanorods are firmly chemisorbed on $Ti_3C_2T_X$ nanosheets to form new chemical bonds, but also reflects their strong chemical adsorption. These results demonstrate that the intercalation strategy of inserting PANI nanorods into the interlayer structure of $Ti_3C_2T_X$ nanosheets is not only feasible but also effective. In the O 1 s spectrum (Fig. 2g), the peaks are deconvoluted into 531.3 (C-O) and 533 eV (C═O) respectively due to the bonding of O and C. Fig. 2h shows the spectrum of Ti 2p, which corresponds to Ti $2p_{3/2}$ and Ti 2 $P_{1/2}$ (451.9 and 458.5 eV), Ti-C $2p_{3/2}$ and Ti-C 2 $P_{1/2}$ (454.4 and 460.7 eV), Ti-N $2p_{3/2}$ and Ti-N $2p_{1/2}$ (455.9 and 462.4 eV), Ti^{4+} $2p_{3/2}$ and Ti^{4+} $2p_{1/2}$ (458.6 and 464.6 eV). These results not only verified the preparation of the composite, but also show the strong chemical adsorption between PANI nanorods and $Ti_3C_2T_X$ nanosheets.

A general view of the reaction to generate the $Ti_3C_2T_X$ @PANI-RGO heterostructure hydrogel as shown in Fig. 3a. The $Ti_3C_2T_X$ @ PANI heterostructures were fitted into the 3D porous cross-linked hydrogel by a low-temperature hydrothermal self-assembly tactic assisted by the strong gelling cross-linking agent GO. Given that $Ti_3C_2T_X$ nanosheets are easily oxidized under high temperature hydrothermal treatment, a mild temperature hydrothermal strategy was chosen to avoid terrible oxidization and structural degeneration of $Ti_3C_2T_X$. At the same time, Vitamin C was selected as the reducing agent, avoiding explosive reducing agents such as hydrazine hydrate.

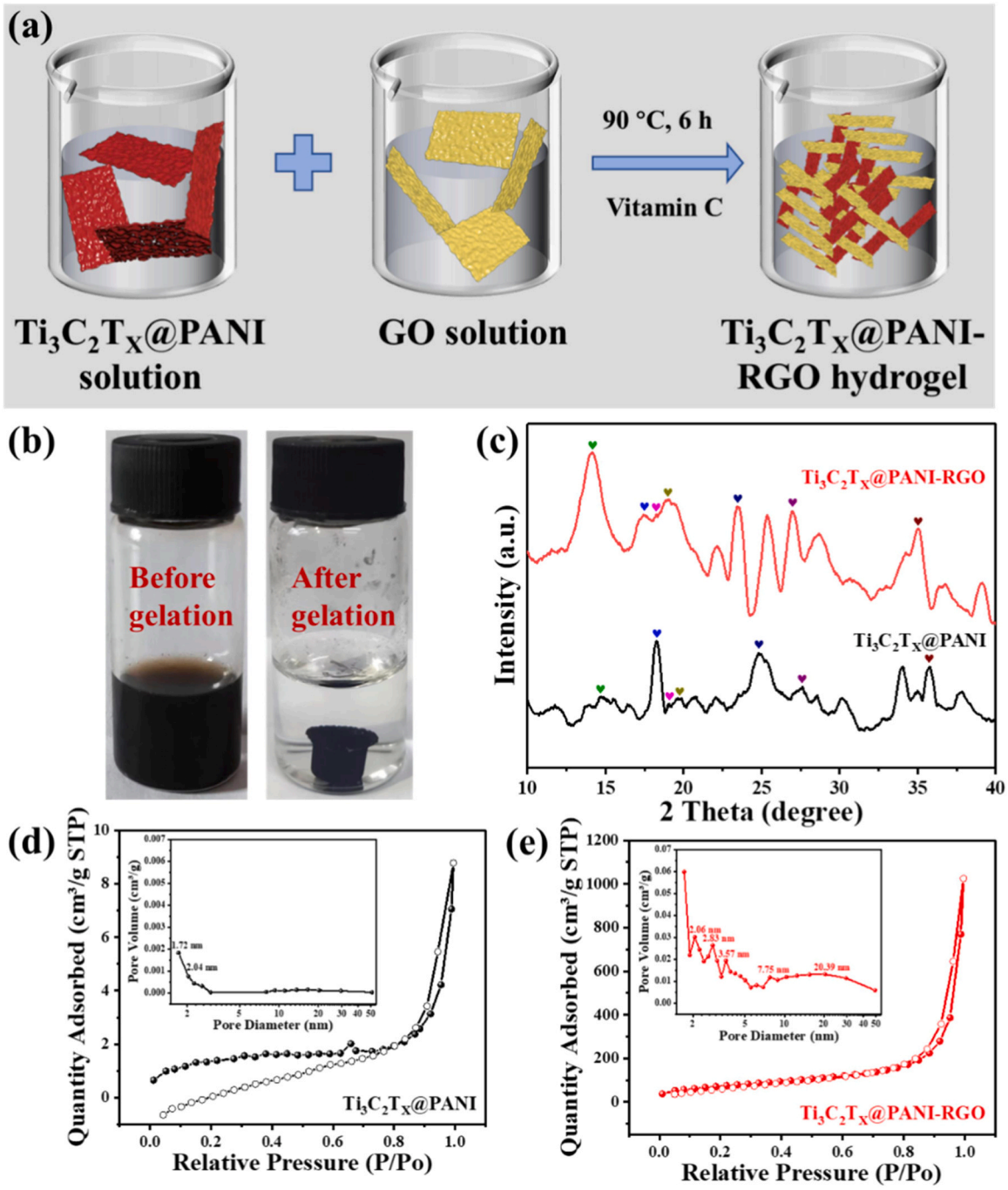

Fig. 3. (a) Schematic illustration of the synthesis of 3D $Ti_3C_2T_X$ @PANI-RGO hydrogel. (b) Photos of a $Ti_3C_2T_X$ @PANI/GO colloid before and after treatment at 90 °C. (c) XRD patterns of $Ti_3C_2T_X$ @PANI and $Ti_3C_2T_X$ @PANI-RGO hydrogel. N_2 adsorption-desorption analysis of (d) $Ti_3C_2T_X$ @PANI powder and (e) $Ti_3C_2T_X$ @PANI-RGO hydrogel.

During the low-temperature hydrothermal self-assembly process, the RGO nanosheets obtained by the reduction of GO with Vitamin C were interconnected with the surface oxygen-containing groups of $Ti_3C_2T_X$ to form 3D $Ti_3C_2T_X$ @PANI-RGO hydrogel. As shown in Fig. 3b, the $Ti_3C_2T_X$ @PANI/GO (66.7%/33.3% mass fraction, respectively) mixed colloidal solution precursor reacted at 90 °C to form 3D hydrogel. XRD patterns of $Ti_3C_2T_X$ @PANI powder (black curve) and $Ti_3C_2T_X$ @PANI-RGO hydrogel (red curve) in Fig. 3c show that after inserting RGO between $Ti_3C_2T_X$ @PANI, the half-peak width of multiple diffraction peaks in $Ti_3C_2T_X$ @PANI-RGO hydrogels became wider, and the peak positions shifted to the left.

N_2 adsorption/desorption tests display that the aggregation of $Ti_3C_2T_X$ @PANI powder was effectively inhibited. Fig. 3d reveals the N_2 adsorption/desorption isotherm of the $Ti_3C_2T_X$ @PANI powder, and it can be found that the adsorption-desorption isotherm crosses phenomenon on account of its small specific surface area. The very low adsorption volume of $Ti_3C_2T_X$ @PANI powder in the medium pressure range indicates that there are no obvious mesopores, while the curve rises in the low-pressure range indicates a certain amount of micropores. In contrast, the adsorption isotherm of $Ti_3C_2T_X$ @PANI-RGO hydrogel rapidly increased in the range of relatively medium and low pressure and appeared a hysteresis loop, which was a typical type IV isotherm, indicating the presence of mesoporous (Fig. 3e). There is an obvious H_2-type hysteresis loop in the relative pressure range of 0.1–1.0, indicating that the pore size distribution is uniform, and the pore shape structure is complex. The

SSA of the $Ti_3C_2T_X$ @PANI-RGO hydrogel calculated according to the BET method is 264.79 $m^2\ g^{-1}$, which is about 60 times that of the $Ti_3C_2T_X$ @PANI powder (4.86 $m^2\ g^{-1}$).

It can be seen in Fig. 3d inset that the main distribution of the $Ti_3C_2T_X$ @PANI powder has a micropore size of 1.72 nm and a mesopore size of 2.04 nm, while the pore volume and mesopore size are 0.0103 $cm^3\ g^{-1}$ and 11.17 nm, respectively. Meanwhile, the pore size distribution of $Ti_3C_2T_X$ @PANI-RGO heterostructure hydrogel is shown in Fig. 3e inset, the main distribution of mesopore pore size is 2.06, 2.83, 3.57, 7.75, and 20.39 nm, the pore volume and mesopore pore size are 1.1843 $cm^3\ g^{-1}$, 23.95 nm, respectively. From Fig. 3d and e inset, we can see that the $Ti_3C_2T_X$ @PANI-RGO heterostructure hydrogel has a larger pore volume than the $Ti_3C_2T_X$ @PANI powder (the ordinate differs by an order of magnitude), and in the mesopore range (2–50 nm) are more distributed. Above results suggest that 3D porous hydrogels with stochastic open pores and filmy pore walls built from $Ti_3C_2T_X$ @PANI and RGO are beneficial for alleviating aggregation, making better use of high conductivity and providing more accessible field of practical application of active substances.

The capacitance characteristics was then tested in the potential range of − 1.0–0.0 V. 3D $Ti_3C_2T_X$ @PANI-RGO hydrogel with high mechanical strength can be directly used as an independent SCs electrode, which excludes the interference of inert binders and conductive agents. CV plots of RGO, $Ti_3C_2T_X$-RGO, and $Ti_3C_2T_X$ @PANI-RGO hydrogel electrodes in a three-electrode system with 1 M KOH at 10 mV s^{-1} as shown in Fig. 4a. All the CV curves are quasi-rectangular, and the CV curves of the hydrogel electrodes show a larger integrated area (about 3.37 times that of RGO and 2.62 times that of $Ti_3C_2T_X$-RGO), indicating that the former has better capacitance performance and faster charge-discharge characteristics. Furthermore, obvious redox peaks appeared in the CV curves of the $Ti_3C_2T_X$ @PANI-RGO hydrogel, indicating a reversible redox reaction during the charge and discharge process in PANI. When the working voltage is at a low value, PANI is in a fully reduced state, called leucoemeraldine (LE); when the working voltage moves to a position of a large value, LE is partially oxidized and its structure becomes an emeraldine (EM) structure; when the working voltage moves further to the position where the value is larger, EM is further oxidized to a fully oxidized state pernigraniline (PE). In the wide working voltage range, PANI typically undergoes 3 redox reactions, including the redox transition between the fully reduced state (insulating) and protonated EM (conducting), the transition between benzoquinone and hydroquinone, and the redox transition between EM and fully oxidized state. When PANI switches between different redox states, the reversible ion doping process occurs by a pseudocapacitive process of energy storage and release. The hydrogel electrode displays the synergistic effect of electric double layer capacitance and pseudocapacitance, which possesses both the high specific capacitance of pseudocapacitors and the stability of circulation of electric double layer capacitance.

Fig. 4b displays the CV curves of the $Ti_3C_2T_X$ @PANI-RGO heterostructure hydrogel electrode at 5–50 mV s^{-1}. All CV plots exhibit a rectangle-like shape, and as the potential scan rate increases, the shape is not appreciably distorted even at ultra-high scan rates, exhibiting remarkable capacitance characteristics. The charge storage capabilities of the electrodes were further analyzed by measuring the GCD plots at of 1 A g^{-1} (Fig. 4c). One can see that the $Ti_3C_2T_X$ @PANI-RGO electrode exhibits a longer discharge time, and the specific capacitance (374.17 F g^{-1}) is clearly higher than those of $Ti_3C_2T_X$-RGO (136.50 F g^{-1}) and RGO (124.30 F g^{-1}). This reveals the enhanced charge storage performance of gelled $Ti_3C_2T_X$ @PANI by the highly conductive 3D RGO framework, which agrees well with the CV data. Furthermore, all GCD plots of those electrodes are quasi-triangular, which indicates the joint contribution of the EDLC of $Ti_3C_2T_X$ and RGO and the pseudocapacitance of PANI.

As shown in Fig. 4d, in the current density range of 0.5–10 A g^{-1}, no apparent IR drop in GCD measurements of $Ti_3C_2T_X$ @PANI-RGO hydrogel is found, showing rapid electron transfer and electrolyte ion diffusion in the electrode sheet. In addition, the slopes of all GCD curves are almost steep during charging and rather gentle during discharging, indicating a good charge-discharge stability, and an excellent performance for rapid charging and long-lasting discharge. As shown in Fig. 4e, the specific capacitances of RGO, $Ti_3C_2T_X$-RGO and $Ti_3C_2T_X$ @PANI-RGO decreased with increasing current densities. Compared to RGO, $Ti_3C_2T_X$ @PANI-RGO has good rate performance at current densities of 2–10 A g^{-1}, while at 0.5–1 A g^{-1} it has a high specific capacitance at the current density. Fig. 4f shows that the specific capacitance of heterostructure hydrogel is as high as 617.84 F g^{-1} at 0.5 A g^{-1}, and retains a specific capacitance of 135.10 F g^{-1} at 10 A g^{-1}. Although the specific capacitance of $Ti_3C_2T_X$ @PANI-RGO at high current density is still considerable, it has a non-negligible decline compared with the specific capacitance at low current density, and the overall rate performance has not met expectations. The following work needs to focus on developing effective strategies to improve the charge/discharge capacity of the hydrogel electrode when working at high current densities. As shown in Table 1, the hydrogel electrode displays a higher specific capacitance than electrodes which based on MXene, etc.

Fig. 4 g displays the EIS results for the samples (the inset is the equivalent circuit). We can detect that the semicircular shapes of RGO, $Ti_3C_2T_X$-RGO, and $Ti_3C_2T_X$ @PANI-RGO hydrogels are similar, with calculated R_{ct} (Reaction resistance, that is, the interface charge transfer resistance in the reaction) of 4.39, 1.77, and 1.47 Ω, respectively, indicating the sequential enhancement of electron transfer kinetics. Furthermore, the R_s (internal resistance) of RGO, $Ti_3C_2T_X$-RGO, and $Ti_3C_2T_X$ @PANI-RGO hydrogels are 2.90, 1.94, and 0.35 Ω, respectively. This indicates that the gelation of $Ti_3C_2T_X$ @PANI indeed enhances the electrical conductivity of the heterostructure, which echoes the aforementioned larger specific surface area and more mesopores. Notably, the slope of the linear segment of $Ti_3C_2T_X$ @PANI-RGO is larger than that of $Ti_3C_2T_X$ @PANI, indicating increasingly capacitive nature of the former. In the Ragone plot (Fig. 4 h), $Ti_3C_2T_X$ @PANI-RGO exhibits the supreme energy density of 85.81 Wh kg^{-1} at 509.35 W kg^{-1}, and even at 12,062.73 W kg^{-1}, it still retains 18.76 Wh kg^{-1}. Cycling stability, a crucial indicator for evaluating the performance of SCs, which was tested by continuous 10,000 charge-discharge processes at a current density of 10 A g^{-1}. From Fig. 4i, one can see that more than 90.74% of the capacitance of $Ti_3C_2T_X$ @PANI-RGO hydrogel is preserved (89.46% for RGO and 88.14% for $Ti_3C_2T_X$-RGO) and the GCD curves don't change obviously, suggesting that the heterostructure hydrogel has the advantages of low leakage current and the stability of circulation.

3.2. Structure and electrochemical characteristics of cathode materials

Because of the good conductivity, abundant mesoporous structure, and high specific surface area, defect-rich RGO has been considered as an ideal cathode material for ASCs. In this study, a defect-rich RGO hydrogel was synthesized through a multi-step co-catalytic gasification strategy outlined in Fig. 5a, first reducing a homogeneously mixed solution of RGO and Co particles, followed by catalytic gasification to create cavities, and finally washing with boiling concentrated nitric acid. In the SEM tests, it can be detected that the RGO nanosheets show a wrinkled morphology (Fig. 5b), and the cross-linked configuration can be clearly seen; on the basis of the above morphology, 3D DRGO has clear mesoporous characteristics and uniformly distributed pores (Fig. 5c and d). The micro-topography was deeply discussed by TEM tests, RGO and DRGO reveal a layered, curled, and paper-like constructure. It can be seen that the graphitic structure of RGO surface is relatively complete before the patterning process (Fig. 5e); after co-catalytic gasification

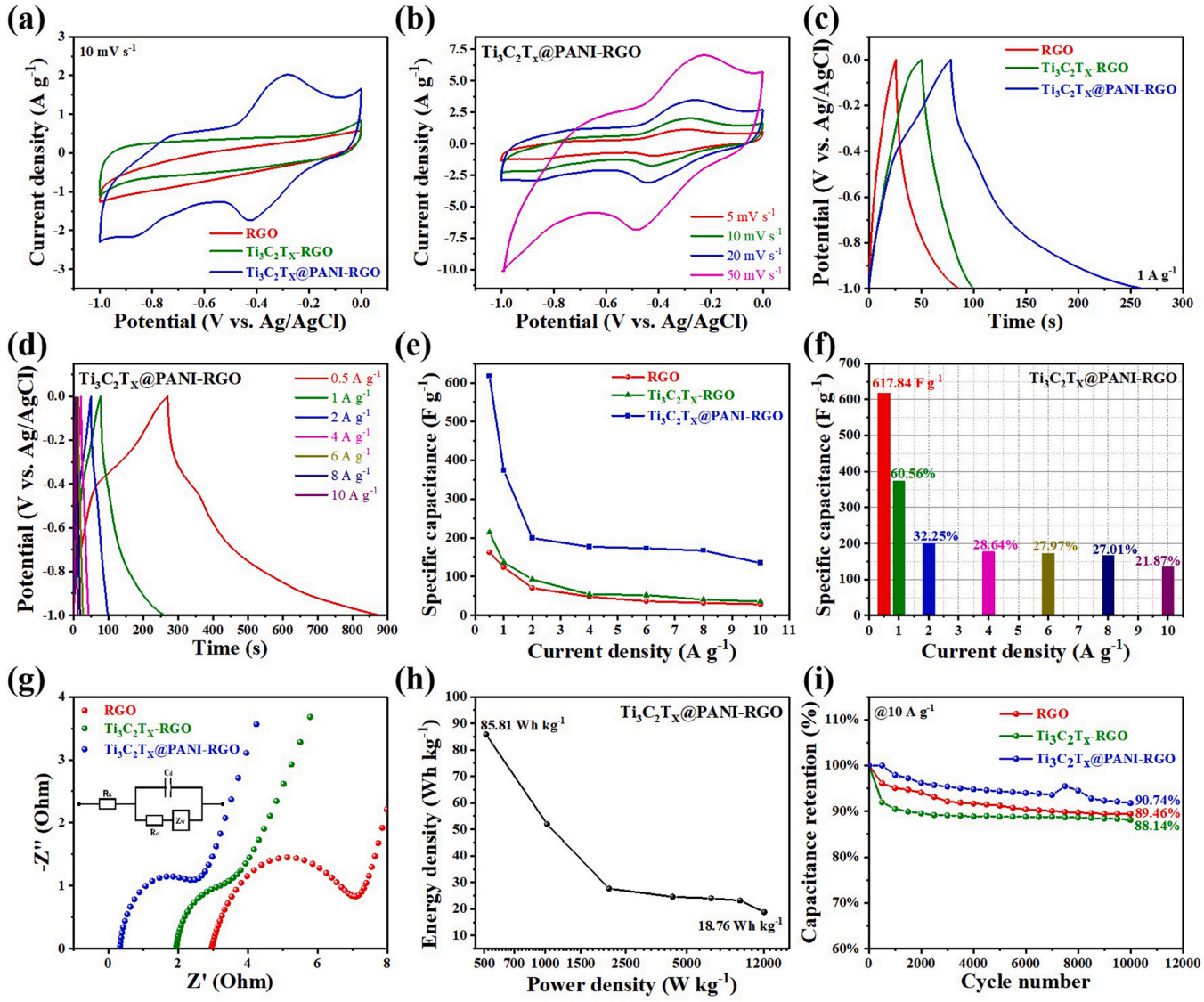

Fig. 4. (a) CV profiles of the electrodes at 10 mV s^{-1}. (b) CV curves of $Ti_3C_2T_X$ @PANI-RGO at 5–50 mV s^{-1}. (c) GCD plots of the electrodes at 1 A g^{-1}. (d) GCD profiles of $Ti_3C_2T_X$ @PANI-RGO. (e) Specific capacitance of the electrodes at different current densities. (f) Specific capacitances vs. various current densities profiles of $Ti_3C_2T_X$ @PANI-RGO. (g) Nyquist impedance plots of the electrodes, with the equivalent circuit shown in the insert. (h) Ragone plot of $Ti_3C_2T_X$ @PANI-RGO. (i) Cycling stability of the electrodes tested at 10 A g^{-1} over 10,000 cycles.

and acid etching, a good deal of cavities are distributed on DRGO surface (Fig. 5f and g). Fig. 5 reflects that through defect engineering, DRGO not only retains the stable graphitic structure like RGO, but also distributes a large number of pores uniformly. Thus, the thermal stability of DRGO is not reduced, and its larger specific surface area can provide higher specific capacitance.

The structural changes of RGO and DRGO were verified by XRD and Raman spectroscopy surveys. The XRD patterns as shown in Fig. 6a, diffraction peaks at 2θ = 25.04° and 43.06° of RGO are assigned to the graphitic (002) and (100) carbon layers (JCPDS 75–1621), respectively, while in DRGO, the half-peak width becomes wider as it moves to the left (2θ = 23.68° and 42.99°). This shows

Table 1
Comparison of charge storage capacity of existing SCs based on MXenes, conductive polymer, and carbon electrodes.

Materials	Electrolyte	Specific capacitance	Current density or Scan rate	Ref.
S-MXene/$HG_{0.05}$	1 M H_2SO_4	446 F g^{-1}	2 mV s^{-1}	[24]
MX-HGH_{20}	1 M H_2SO_4	415 F g^{-1}	1 A g^{-1}	[27]
V_2CT_X	simulating seawater solution	91.3 F g^{-1}	1 A g^{-1}	[29]
PrGO/HKUST-1	1 M KCl/PVA	360.5 F g^{-1}	5 mV s^{-1}	[40]
rGO/Zn-MOF@PANI	1 M H_2SO_4	372 F g^{-1}	0.1 A g^{-1}	[41]
rGO/Cu-MOF@PANI	1 M H_2SO_4	276 F g^{-1}	0.5 A g^{-1}	[42]
ZIF-8/PANI	PVA–1 M H_2SO_4 Gel	395.4 F g^{-1}	0.2 A g^{-1}	[44]
PAN/γ-CD-MOF carbon	1 M H_2SO_4	283.3 F g^{-1}	0.5 A g^{-1}	[46]
Cu-MOF-rGO	1 M Na_2SO_4	366.6 F g^{-1}	1 A g^{-1}	[51]
ZrO_2/C	PVA/1 M 1 M H_2SO_4	241.5 F g^{-1}	1 A g^{-1}	[52]
$Ti_3C_2T_x$ @PANI-RGO	1 M KOH	617.84 F g^{-1}	0.5 A g^{-1}	This work

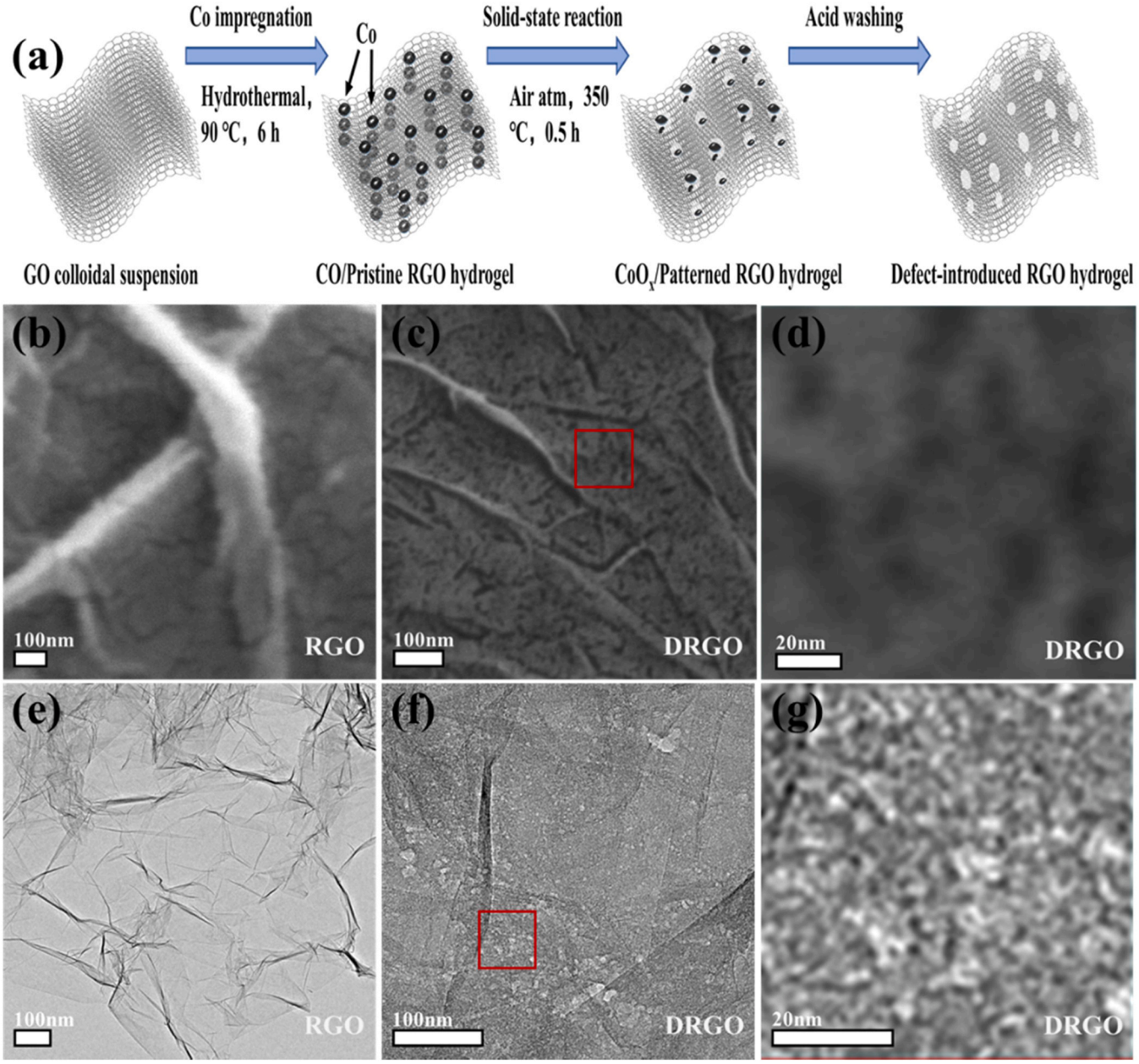

Fig. 5. (a) Schematic diagram for the synthesis process of DRGO hydrogel. SEM images of (b) RGO and (c) DRGO. (d) Zoom-in view of dashed region in (c). TEM images of (e) RGO and (f) DRGO. Enlarged TEM image (g) is cropped from the area in (f).

that, compared with RGO, DRGO can better suppress the stacking of carbon layers. Fig. 6b shows the corresponding Raman spectra of RGO and DRGO. It can be seen that the D peak located near 1350 cm^{-1} represents the sp^2 site, the G peak located near 1586 cm^{-1} represents the $E_{2\,g}$ vibrational mode in the aromatic carbocyclic ring and the 2D peak near 2697 cm^{-1} represents the out-of-plane mode of the aromatic carbocyclic ring. Since the D peak attributes to the disordered sp^2 carbon induced by attachment to the sp^3 carbon atom, it does not appear in the perfect graphitic structure. Hence, the D and G peak intensity ratio of DRGO (I_D/I_G = 1.15) is significantly larger than that of RGO (I_D/I_G = 0.92), confirming that the former has more structural defects.

Fig. 6c and d depict the N_2 adsorption-desorption isotherms for RGO and DRGO. The original RGO isotherm is a type II isotherm with a rapidly rising curve under low relative pressure, with a certain amount of macropore distribution (Fig. 6c). As a comparison, DRGO shows the characteristic hysteresis loop of the type IV isotherm in the intermediate relative pressure range, which is attributed to the formation of mesopores (Fig. 6d). The hysteresis loop of RGO belongs to the H1 type, showing that a uniform pore size distribution and a regular pore shape. The calculated BET SSA of the DRGO is 78.73 $m^2\ g^{-1}$, markedly higher than that (31.97 $m^2\ g^{-1}$) of pristine RGO. In Fig. 6e, one can see that the main distribution mesopore size of RGO is 3.44 and 35.12 nm, the macropore size is 186.00 nm, while the main pore size is 3.44 nm. Meanwhile, the pore size distribution of the 3D DRGO hydrogel is shown in Fig. 6f, the main distribution of mesopore pore size is 3.42, 7.79, 17.56, and 30.86 nm, while the main pore size is 3.42 nm. Compared to Fig. 6e and f, the 3D DRGO hydrogel has a larger pore volume than the RGO (the ordinate differs by an order of magnitude), and it is in the mesopore range (2–50 nm) and is more widely distributed, which suggest that 3D DRGO is beneficial to alleviate aggregation.

The TGA profiles of the samples are shown in Fig. 7a, and RGO and DRGO end up with 72.67% and 48.23% of the weight remaining,

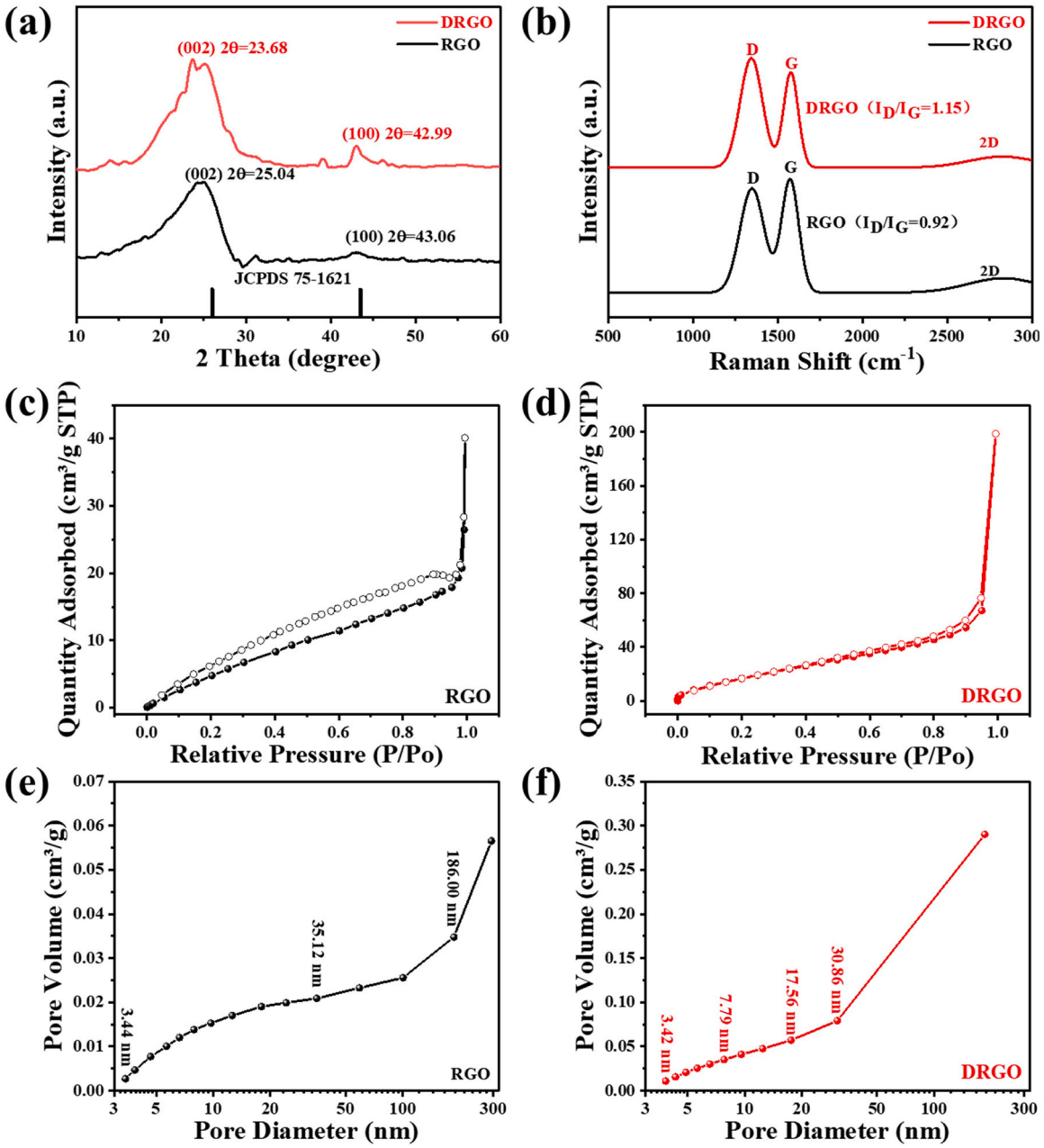

Fig. 6. Spectral characteristics of RGO and DRGO: (a) XRD patterns. (b) Raman spectrum. (c, d) N_2 adsorption-desorption isotherms. (e, f) Pore size distribution.

respectively. Before about 260.93 °C, RGO and DRGO had similar weight loss, and after that, RGO has a sharper curve decline than RGO, indicating a better thermal stability of DRGO. This is because that the unstable groups on the edge of RGO that are easy to absorb water will be easily decomposed at high temperature, while DRGO can dissociate these groups after the reaction of high temperature and washing step, significantly improving its own thermal stability. The capacitive performances of these samples were compared by CV, GCD, and EIS. CV plots of RGO and DRGO at 10 mV s^{-1} are quasi-rectangular as displayed in Fig. 7b. Compared with the RGO electrode, DRGO electrode has a larger integration area (about 2.86 times than that of RGO), reflecting a larger charge storage and a more stable charge-discharge process. Fig. 7c exhibits the CV plots of DRGO electrode at 5, 10, 20, and 50 mV s^{-1}. These CV plots display a rectangular shape and there is no clear distortion as increasing scan rates, showing excellent capacitive properties. The capacitance characteristics of RGO and DRGO was deeply assessed by GCD measurements at a unified current density of 1 A g^{-1}. In Fig. 7d, one can see that the specific capacitance (237.62 F g^{-1}) of the DRGO hydrogel is much larger than that of RGO, which indicates that the formation of defects through the Co catalyzed gasification treatment can improve the charge storage performance.

In Fig. 7e, GCD curves of DRGO hydrogel have no obvious IR drop from 0.5–10 A g^{-1}, revealing good capacitive property. Additionally, GCD curve of DRGO is triangular-like and steep during charging and gentle during discharging, indicating that it takes short time to charge and long time to discharge. These results in Fig. 7b-e imply that the DRGO hydrogel electrodes exhibit typical highly reversible EDLCs properties. Fig. 7f displays the specific capacitance as a function of current density for RGO and DRGO. DRGO has high specific capacitances of 237.62 F g^{-1} at 0.5 A g^{-1} (158.27 F g^{-1} at 10 A g^{-1}, 66.60% retention), while RGO retains only 17.42% of the capacitance. Moreover, the defect structure would not reduce the conductivity of DRGO.

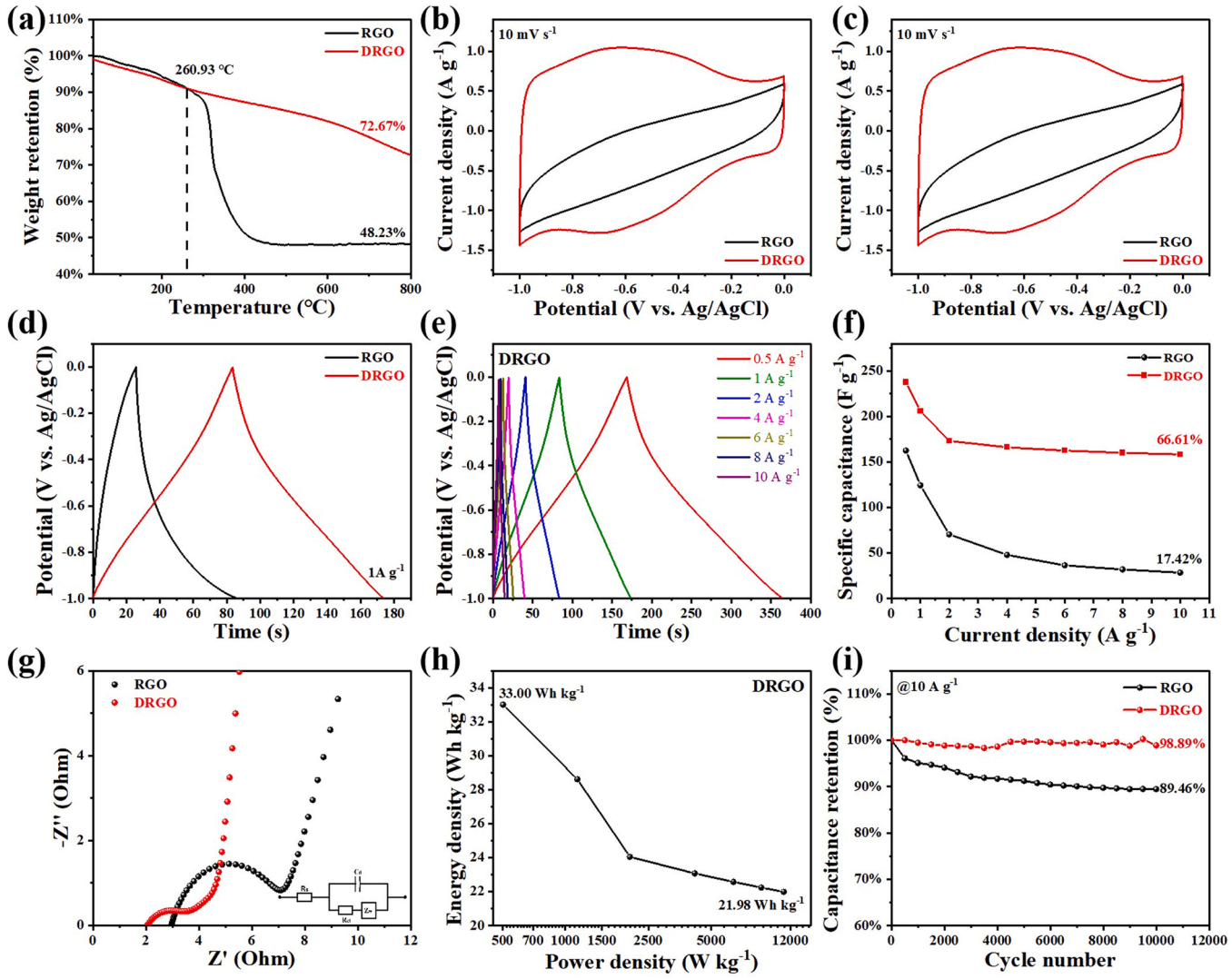

Fig. 7. (a) TG-analysis of the samples. Capacitive characterizations of the samples: (b) CV plots at 10 mV s^{-1}. (c) CV plots of DRGO at 5–50 mV s^{-1}. (d) GCD plots at 1 A g^{-1}. (e) GCD plots of DRGO at 0.5–10 A g^{-1}. (f) Rate capabilities based on GCD plots. (g) Nyquist plots (insert shows the equivalent circuit). (h) Ragone plot of DRGO. (i) Cycling stability.

From Nyquist plot in Fig. 7g (the inset is the equivalent circuit diagram), it can be seen that the R_{ct} (1.70 Ω) and R_s (1.86 Ω) of the DRGO hydrogel are lower compared with that of RGO, and a more vertical line, indicating that the electrochemical impedance of the DRGO hydrogel is lower and the capacitance is better. Furthermore, this indicates that catalytic gasification occurs only on carbon interacting with CoO_X particles, while the basic structures and remarkable electrical conductivity of graphitic carbon are preserved. In Fig. 7h, the DRGO displays a supreme energy density of 33.00 Wh kg^{-1} at 503.42 W kg^{-1}, and at 11,145.79 W kg^{-1}, it also keeps 21.98 Wh kg^{-1}. Subsequently, the cycling property of these electrodes was tested at 10 A g^{-1} by repeated GCD process (Fig. 7i). The DRGO electrode exhibited a much higher capacitance retention rate of 98.89% than that of RGO electrode after 10,000 cycles, indicating a better long-term stability of DRGO electrode.

3.3. $Ti_3C_2T_X$ @PANI-RGO//DRGO ASC

To research the energy storage applications of the active materials for SCs, an ASC device was constructed by using the $Ti_3C_2T_X$ @PANI-RGO hydrogel as anode, DRGO hydrogel as cathode, along with a porous polymer membrane as the separator (Fig. 8a). It is well known that the device exhibits the best electrochemical performance when the charges of anode and cathode are conserved. Thus, the weight ratio of $Ti_3C_2T_X$ @PANI-RGO to DRGO was about 1:2.7 (total of the active materials is approximately 3.70 mg). In Fig. 8b, the potential window of $Ti_3C_2T_X$ @PANI-RGO electrode was − 0.8–0.2 V, while the voltage range of DRGO electrode was − 1.6 to − 0.6 V, which greatly determines the voltage window of the $Ti_3C_2T_X$ @PANI-RGO//DRGO ASC device. Fig. 8c exhibits CV profiles of the ASC device within voltage ranges (−1.0 to 0.0 V, −1.2 to 0.0 V, −1.4 to 0.0 V, −1.6 to 0.0 V, −1.6 to 0.2 V, −1.6 to 0.4 V, and −1.8 to 0.2 V) at 50 mV s^{-1}. Significantly, CV profiles are not closed or crossed within the working voltages are − 1.6–0.4 and − 1.8–0.8 V, respectively (shown in the two dotted boxes), while the CV curve is still not deformed when the voltage window is − 1.6–0.2 V, indicating the operating voltage of the device will be stably expanded to 1.8 V. Typical CV plots of the device (Fig. 8d), in which distinct redox peaks appear caused by the invertible Faraday reaction.

The pseudocapacitive property of this kind of the $Ti_3C_2T_X$ @PANI-RGO//DRGO ASC electrode material is likewise reflected in the GCD curves (Fig. 8e), and which shows similar curvatures. Moreover, there are no evident IR drops in GCD curve, and the quasi-right-angled triangle once again confirms the excellent performance of the $Ti_3C_2T_X$ @PANI-RGO//DRGO ASC device with short charging time and long discharging time. In Fig. 8 f, the specific capacitance of the ASC

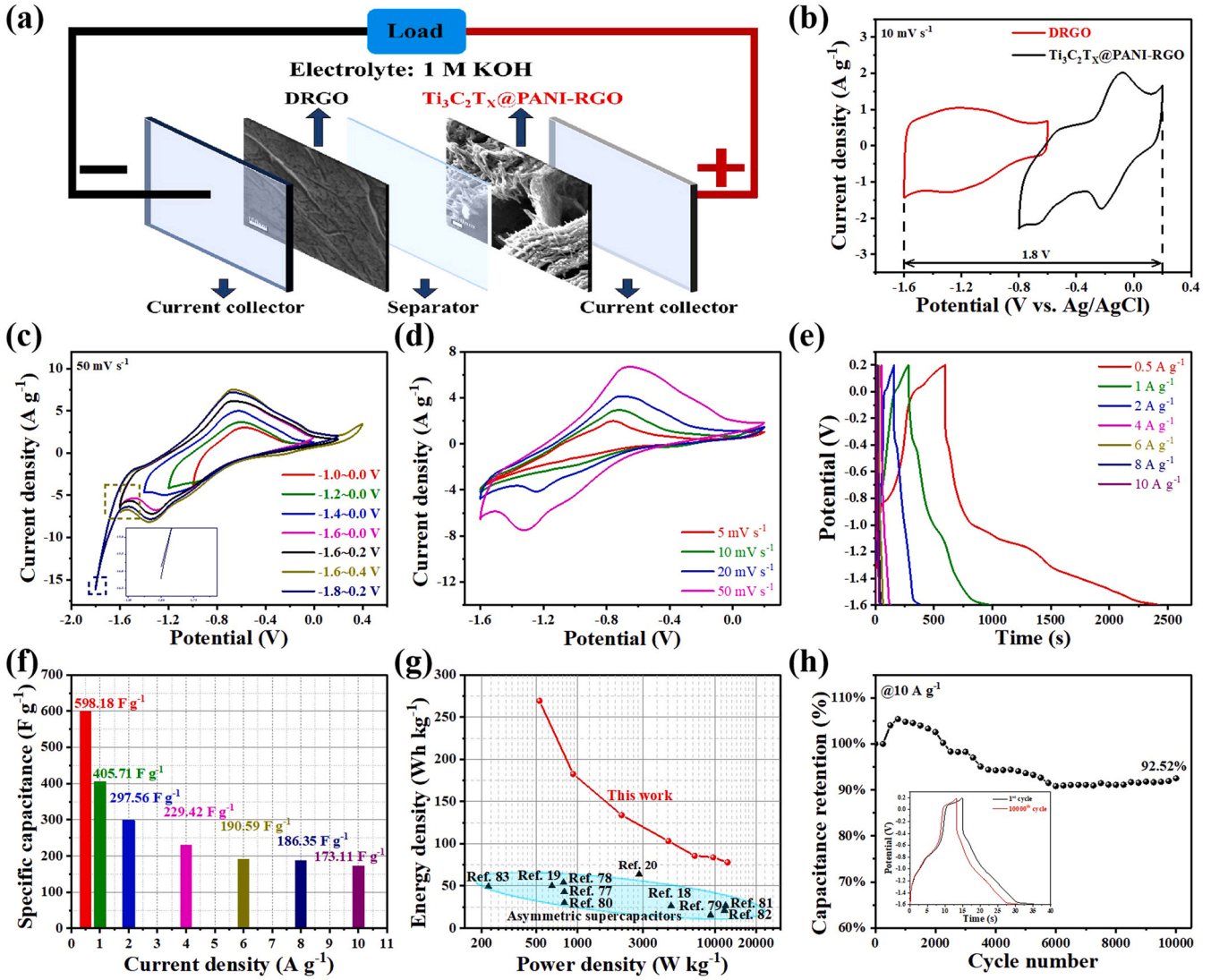

Fig. 8. Capacitance performance of the asymmetric device: (a) Diagrammatical construction of the device. (b) CV profiles of $Ti_3C_2T_X$ @PANI-RGO and DRGO at 10 mV s^{-1}. (c) CV profiles of the device with a series of voltage ranges at 50 mV s^{-1}. (d) CV profiles. (e) GCD profiles. (f) Specific capacitances calculated from the GCD profiles. (g) Ragone plot of power density vs. energy density. (h) Cycling stability of this device over 10,000 cycles at 10 A g^{-1} (inset displays charge–discharge curves for the 1st and 10000th charge–discharge cycles).

device was valuated from the GCD profiles, which are 598.18 F g^{-1} at 0.5 A g^{-1} and 173.11 F g^{-1} at 10 A g^{-1}. Thus, outstanding performance could be due to the matching of capacitances and the balance of rapid redox kinetics. As shown in the Ragone diagram (Fig. 8g), the device shows an ultra-high energy density of 269.18 Wh kg^{-1} at 527.72 W kg^{-1} and retained 77.90 Wh kg^{-1} at 12,409.04 W kg^{-1}. It is obviously found that the Ragone curve of the ASC is much higher than the confidence interval of the Ragone curve of similar ASCs, indicating that this ASC has a much higher energy density than similar ASCs [18–20,77–83]. The ultrahigh energy density exhibited by $Ti_3C_2T_X$ @PANI-RGO//DRGO ASC verifies the feasibility of increasing the energy density by expanding the potential window. As shown in Fig. 8 h, the cycling stability of the device was probed over 10,000 times and retained 92.52% of the initial capacitance and the final GCD curve is basically the same shape as the initial GCD curve (Fig. 8 h inset), indicating remarkable cycling stability.

4. Conclusion

In brief, 3D porous cross-linked $Ti_3C_2T_X$ @PANI-RGO heterostructure hydrogel was prepared through a simple tactic. By chemical adsorption and polymer polymerization, the rod-like polymer material PANI was anchored onto the surface of the 2D $Ti_3C_2T_X$ substrate with high conductivity, forming $Ti_3C_2T_X$ @PANI heterostructure. Then, the composite was assembled with RGO into a 3D porous framework by a GO-assisted self-converging strategy at low temperature. The 3D cross-linked structures effectively suppress the agglomeration of $Ti_3C_2T_X$ @PANI, resulting in a high specific capacitance up to 617.84 F g^{-1} at 0.5 A g^{-1}. At the same time, the catalytic gasification of Co particles can generate defects for the RGO hydrogel synthesized by the low temperature hydrothermal treatment, and then through acid washing, the 3D layered DRGO with abundant and uniform surface pores can be prepared. The DRGO hydrogels exhibit a specific capacitance of 237.62 F g^{-1} at 0.5 A g^{-1} and 158.27 F g^{-1} (66.61% retention) at 10 A g^{-1}. $Ti_3C_2T_X$ @PANI-RGO hydrogel and DRGO hydrogel were used as anode and cathode to construct an ASC device with a voltage range of 1.8 V, and the $Ti_3C_2T_X$ @PANI-RGO//DRGO ASC device shows an ultra-high energy density of 269.18 Wh kg^{-1} at 527.72 W kg^{-1} and even retained an energy density of 77.90 Wh kg^{-1} at 12,409.04 W kg^{-1}. Furthermore, the 92.52% capacitance since 10,000 cycles at 10 A g^{-1}, which reveals a durable cycling stability of the device. This paper points out a

creative policy for the project and production of 3D MXene-based heterostructure hydrogels as positive electrodes and DRGO hydrogel as negative electrodes to assemble advanced ASCs device.

CRediT authorship contribution statement

Peng Liao and Zenghui Qiu devised the concept. Peng Liao and Yang Zeng performed the main experiments and wrote the draft of the manuscript. Peng Liao, Shengcai Hao and Jiaqi He participated in the analysis of the experimental results. Zenghui Qiu, Jiaqi He, Haijun Xu, and Shaowei Chen supervised the research and revised the manuscript. All authors given approval to the final version of the manuscript.

Data availability

Data will be made available on request.

Declaration of Competing Interest

The authors declare that they have no known competing financial interests or personal relationships that could have appeared to influence the work reported in this paper.

Acknowledgements

The financial support from the National Natural Science Foundation of China (52073022 and 31961133017), the National Basic Research Program of China (52014CB745100), the Beijing Natural Science Foundation (4222073), and the National Science Foundation, United States (CHE-1900235) is gratefully acknowledged.

Appendix A. Supporting information

Supplementary data associated with this article can be found in the online version at doi:10.1016/j.jallcom.2023.169593.

References

[1] X. Wei, C.-C. Lin, C. Wu, N. Qaiser, Y. Cai, A.-Y. Lu, K. Qi, J.-H. Fu, Y.-H. Chiang, Z. Yang, L. Ding, O.S. Ali, W. Xu, W. Zhang, M.B. Hassine, J. Kong, H.-Y. Chen, V. Tung, Three-dimensional hierarchically porous MoS_2 foam as high-rate and stable lithium-ion battery anode, Nat. Commun. 13 (2022) 6006.
[2] P. Simon, Y. Gogotsi, Perspectives for electrochemical capacitors and related devices, Nat. Mater. 19 (2020) 1151–1163.
[3] T.M. Gur, Review of electrical energy storage technologies, materials and systems: challenges and prospects for large-scale grid storage, Energy Environ. Sci. 11 (2018) 2696–2767.
[4] Y. Manoharan, S.E. Hosseini, B. Butler, H. Alzhahrani, B.T. Fou, T. Ashuri, J. Krohn, Hydrogen Fuel Cell Vehicles; Current Status and Future Prospect, Appl. Sci. -Basel 9 (2019) 2296.
[5] P.E. Brockway, A. Owen, L.I. Brand-Correa, L. Hardt, Estimation of global final-stage energy-return-on-investment for fossil fuels with comparison to renewable energy sources, Nat. Energy 4 (2019) 612–621.
[6] C. Tarhan, M.A. Cil, A study on hydrogen, the clean energy of the future: Hydrogen storage methods, J. Energy Storage 40 (2021) 102676.
[7] L.B. Dong, W. Yang, W. Yang, Y. Li, W.J. Wu, G.X. Wang, Multivalent metal ion hybrid capacitors: a review with a focus on zinc-ion hybrid capacitors, J. Mater. Chem. A 7 (2019) 13810–13832.
[8] B. Li, J.S. Zheng, H.Y. Zhang, L.M. Jin, D.J. Yang, H. Lv, C. Shen, A. Shellikeri, Y.R. Zheng, R.Q. Gong, J.P. Zheng, C.M. Zhang, Electrode materials, electrolytes, and challenges in nonaqueous lithium-ion capacitors, Adv. Mater. 30 (2018) 1705670.
[9] J. Libich, J. Maca, J. Vondrak, O. Cech, M. Sedlarikova, Supercapacitors: Properties and applications, J. Energy Storage 17 (2018) 224–227.
[10] C. Choi, D.S. Ashby, D.M. Butts, R.H. DeBlock, Q.L. Wei, J. Lau, B. Dunn, Achieving high energy density and high power density with pseudocapacitive materials, Nat. Rev. Mater. 5 (2020) 5–19.
[11] M.Z. Iqbal, U. Aziz, Supercapattery: Merging of battery-supercapacitor electrodes for hybrid energy storage devices, J. Energy Storage 46 (2022) 103823.
[12] R. Vanaraj, R. Vinodh, T. Periyasamy, S. Madhappan, C.M. Babu, S.P. Asrafali, R. Haldhar, C.J. Raorane, H. Hwang, H.J. Kim, M. Yi, S.C. Kim, Capacitance Enhancement of Metal-Organic Framework (MOF) Materials by Their Morphology and Structural Formation, Energy Fuels 36 (2022) 4978–4991.
[13] M.H. Hamsan, S.B. Aziz, M.F.Z. Kadir, M.A. Brza, W.O. Karim, The study of EDLC device fabricated from plasticized magnesium ion conducting chitosan based polymer electrolyte, Polym. Test. 90 (2020) 106714.
[14] T. Li, R. Ma, J.H. Lin, Y.P. Hu, P.X. Zhang, S.C. Sun, L. Fang, The synthesis and performance analysis of various biomass-based carbon materials for electric double-layer capacitors: A review, Int. J. Energy Res. 44 (2020) 2426–2454.
[15] S.X. Yan, S.H. Luo, J. Feng, P.W. Li, R. Guo, Q. Wang, Y.H. Zhang, Y.G. Liu, S. Bao, Rational design of flower-like $FeCo_2S_4$/reduced graphene oxide films: Novel binder-free electrodes with ultra-high conductivity flexible substrate for high-performance all-solid-state pseudocapacitor, Chem. Eng. J. 381 (2020) 122695.
[16] T.F. Yi, L.Y. Qiu, J. Mei, S.Y. Qi, P. Cui, S.H. Luo, Y.R. Zhu, Y. Xie, Y.B. He, Porous spherical NiO@$NiMoO_4$@PPy nanoarchitectures as advanced electrochemical pseudocapacitor materials, Sci. Bull. 65 (2020) 546–556.
[17] B. Yao, S. Chandrasekaran, J. Zhang, W. Xiao, F. Qian, C. Zhu, E.B. Duoss, C.M. Spadaccini, M.A. Worsley, Y. Li, Efficient 3D Printed Pseudocapacitive Electrodes with Ultrahigh MnO_2 Loading, Joule 3 (2019) 459–470.
[18] S. Cheng, T. Shi, C. Chen, Y. Zhong, Y. Huang, X. Tao, J. Li, G. Liao, Z. Tang, Construction of porous $CuCo_2S_4$ nanorod arrays via anion exchange for high-performance asymmetric supercapacitor, Sci. Rep. 7 (2017) 6681.
[19] M. Safari, J. Mazloom, K. Boustani, A. Monemdjou, Hierarchical Fe_2O_3 hexagonal nanoplatelets anchored on SnO_2 nanofibers for high-performance asymmetric supercapacitor device, Sci. Rep. 12 (2022) 14919.
[20] S. Nagamuthu, K.S. Ryu, Synthesis of Ag/NiO honeycomb structured nanoarrays as the electrode material for high performance asymmetric supercapacitor devices, Sci. Rep. 9 (2019) 4864.
[21] J.Y. Heo, R. Vinodh, H.J. Kim, R.S. Babu, K.K. Kumar, C. Gopi, S. Kim, Template and binder free 1D cobalt nickel hydrogen phosphate electrode materials for supercapacitor application, J. Ind. Eng. Chem. 106 (2022) 328–339.
[22] J.B. Cheng, C.L. Wang, X.M. Zou, L. Liao, Recent Advances in Optoelectronic Devices Based on 2D Materials and Their Heterostructures, Adv. Opt. Mater. 7 (2019) 1800441.
[23] H.B. Sun, J.C. Dong, F.N. Liu, F. Ding, Etching of two-dimensional materials, Mater. Today 42 (2021) 192–213.
[24] Z. Cai, Y.F. Ma, M. Wang, A.N. Qian, Z.M. Tong, L.T. Xiao, S.T. Jia, X.Y. Chen, Engineering of electrolyte ion channels in MXene/holey graphene electrodes for superior supercapacitive performances, Rare Met. 41 (2022) 2084–2093.
[25] Y. Ai, W. Li, D.Y. Zhao, Special Topic: Two-dimensional Functional Materials 2D mesoporous materials, Natl. Sci. Rev. (9) (2022) nwab108.
[26] G.H. Jeong, S.P. Sasikala, T. Yun, G.Y. Lee, W.J. Lee, S.O. Kim, Nanoscale Assembly of 2D Materials for Energy and Environmental Applications, Adv. Mater. 32 (2020) 1907006.
[27] Z.X. Zhu, Z.X. Wang, Z.H. Ba, X.T. Li, J. Dong, Y.T. Fang, Q.H. Zhang, X. Zhao, 3D MXene-holey graphene hydrogel for supercapacitor with superior energy storage, J. Energy Storage 47 (2022) 103911.
[28] W.L. Xu, X. Zhao, F.Y. Zhan, Q.Q. He, H.Y. Wang, J. Chen, H.Y. Wang, X.H. Ren, L.Y. Chen, Toward emerging two-dimensional nickel-based materials for electrochemical energy storage: Progress and perspectives, Energy Storage, Materials 53 (2022) 79–135.
[29] H.T. He, Q.X. Xia, B.X. Wang, L.B. Wang, Q.K. Hu, A.G. Zhou, Two-dimensional vanadium carbide (V_2CT_X) MXene as supercapacitor electrode in seawater electrolyte, Chin. Chem. Lett. 31 (2020) 984–987.
[30] K. Li, M.Y. Liang, H. Wang, X.H. Wang, Y.S. Huang, J. Coelho, S. Pinilla, Y.L. Zhang, F.W. Qi, V. Nicolosi, Y.X. Xu, 3D MXene Architectures for Efficient Energy Storage and Conversion, Adv. Funct. Mater. 30 (2020) 2000842.
[31] R.P. Pandey, K. Rasool, V.E. Madhavan, B. Aissa, Y. Gogotsi, K.A. Mahmoud, Ultrahigh-flux and fouling-resistant membranes based on layered silver/MXene ($Ti_3C_2T_X$) nanosheets, J. Mater. Chem. A 6 (2018) 3522–3533.
[32] Y.M. Wang, X. Wang, X.L. Li, Y. Bai, H.H. Xiao, Y. Liu, R. Liu, G.H. Yuan, Engineering 3D Ion Transport Channels for Flexible MXene Films with Superior Capacitive Performance, Adv. Funct. Mater. 29 (2019) 1900326.
[33] Y.M. Wang, X. Wang, X.L. Li, Y. Bai, H.H. Xiao, Y. Liu, G.H. Yuan, Scalable fabrication of polyaniline nanodots decorated MXene film electrodes enabled by viscous functional inks for high-energy-density asymmetric supercapacitors, Chem. Eng. J. 405 (2021) 126664.
[34] L.H. Yu, Z.D. Fan, Y.L. Shao, Z.N. Tian, J.Y. Sun, Z.F. Liu, Versatile N-Doped MXene Ink for Printed Electrochemical Energy Storage Application, Advanced Energy, Materials 9 (2019) 1901839.
[35] M. Alhabeb, K. Maleski, T.S. Mathis, A. Sarycheva, C.B. Hatter, S. Uzun, A. Levitt, Y. Gogotsi, Selective Etching of Silicon from Ti_3SiC_2 (MAX) To Obtain 2D Titanium Carbide (MXene), Angew. Chem. -Int. Ed. 57 (2018) 5444–5448.
[36] L.Y. Yu, L.F. Hu, B. Anasori, Y.T. Liu, Q.Z. Zhu, P. Zhang, Y. Gogotsi, B. Xu, MXene-Bonded Activated Carbon as a Flexible Electrode for High-Performance Supercapacitors, Acs Energy Lett. 3 (2018) 1597–1603.
[37] C.L. Liu, Y. Bai, W.T. Li, F.Y. Yang, G.X. Zhang, H. Pang, In Situ Growth of Three-Dimensional MXene/Metal-Organic Framework Composites for High-Performance Supercapacitors, Angew. Chem. -Int. Ed. 61 (2022) e202116282.
[38] C.L. Hou, H.Z. Yu, ZnO/$Ti_3C_2T_X$ monolayer electron transport layers with enhanced conductivity for highly efficient inverted polymer solar cells, Chem. Eng. J. 407 (2021) 127192.
[39] D.B. Xiong, X.F. Li, Z.M. Bai, S.G. Lu, Recent Advances in Layered $Ti_3C_2T_X$ MXene for Electrochemical Energy Storage, Small 14 (2018) 1703419.
[40] D. Mohanadas, M. Abdah, N.H.N. Azman, T. Ravoof, Y. Sulaiman, Facile synthesis of PEDOT-rGO/HKUST-1 for high performance symmetrical supercapacitor device, Sci. Rep. 11 (2021) 11747.

[41] L.Q. Bao, T.H. Nguyen, H.J. Fei, I. Sapurina, F.A. Ngwabebhoh, C. Bubulinca, L. Munster, E.D. Bergerova, A. Lengalova, H. Jiang, T.T. Dao, N. Bugarova, M. Omastova, N.E. Kazantseva, P. Saha, Electrochemical performance of composites made of rGO with Zn-MOF and PANI as electrodes for supercapacitors, Electrochim. Acta 367 (2021) 137563.
[42] Q.B. Le, T.H. Nguyen, H.J. Fei, C. Bubulinca, L. Munster, N. Bugarova, M. Micusik, R. Kiefer, T.T. Dao, M. Omastova, N.E. Kazantseva, P. Saha, Electrochemical performance of composite electrodes based on rGO, Mn/Cu metal-organic frameworks, and PANI, Sci. Rep. 12 (2022) 664.
[43] J. Guo, Z.R. Chen, X.J. Xu, X. Li, H. Liu, S.H. Xi, W. Abdul, Q. Wu, P. Zhang, B.B. Xu, J.F. Zhu, Z.H. Guo, Enhanced electromagnetic wave absorption of engineered epoxy nanocomposites with the assistance of polyaniline fillers, Advanced Composites and Hybrid, Materials 5 (2022) 1769–1777.
[44] A.P.M. Udayan, O. Sadak, S. Gunasekaran, Metal-organic framework/polyaniline nanocomposites for lightweight energy storage, ACS Appl. Energy Mater. 3 (2020) 12368–12377.
[45] M.A. Deshmukh, R. Celiesiute, A. Ramanaviciene, M.D. Shirsat, A. Ramanavicius, EDTA_PANI/SWCNTs nanocomposite modified electrode for electrochemical determination of copper (II), lead (II) and mercury (II) ions, Electrochim. Acta 259 (2018) 930–938.
[46] W. Xu, L.H. Wang, Y. Chen, Y. Liu, Flexible carbon membrane supercapacitor based on gamma-cyclodextrin-MOF, Materials Today, Chemistry 24 (2022) 100896.
[47] Y. Ma, C.P. Hou, H.P. Zhang, Q.Y. Zhang, H. Liu, S.D. Wu, Z.H. Guo, Three-dimensional core-shell Fe_3O_4/Polyaniline coaxial heterogeneous nanonets: Preparation and high performance supercapacitor electrodes, Electrochim. Acta 315 (2019) 114–123.
[48] A. Atta, M.M. Abdelhamied, A.M. Abdelreheem, N.A. Althubiti, Effects of polyaniline and silver nanoparticles on the structural characteristics and electrical properties of methylcellulose polymeric films, Inorg. Chem. Commun. 135 (2022) 109085.
[49] S. Korkmaz, I.A. Kariper, Graphene and graphene oxide based aerogels: Synthesis, characteristics and supercapacitor applications, J. Energy Storage 27 (2020) 101038.
[50] A.T. Lawal, Graphene-based nano composites and their applications. A review, Biosens. Bioelectron. 141 (2019) 111384.
[51] M.K. Singh, A.K. Gupta, S. Krishnan, N. Guha, S. Marimuthu, D.K. Rai, A new hierarchically porous Cu-MOF composited with rGO as an efficient hybrid supercapacitor electrode material, J. Energy Storage 43 (2021) 103301.
[52] V. Shrivastav, S. Sundriyal, U.K. Tiwari, K.H. Kim, A. Deep, Metal-organic framework derived zirconium oxide/carbon composite as an improved supercapacitor electrode, Energy 235 (2021) 121351.
[53] M.B. Arvas, H. Gursu, M. Gencten, Y. Sahin, Preparation of different heteroatom doped graphene oxide based electrodes by electrochemical method and their supercapacitor applications, J. Energy Storage 35 (2021) 102328.
[54] J.F. Wu, Q.E. Zhang, J.J. Wang, X.P. Huang, H. Bai, A self-assembly route to porous polyaniline/reduced graphene oxide composite materials with molecular-level uniformity for high-performance supercapacitors, Energy Environ. Sci. 11 (2018) 1280–1286.
[55] R. Kumar, S. Sahoo, E. Joanni, R.K. Singh, W.K. Tan, K.K. Kar, A. Matsuda, Recent progress in the synthesis of graphene and derived materials for next generation electrodes of high performance lithium ion batteries, Prog. Energy Combust. Sci. 75 (2019) 100786.
[56] K. Poonam, A. Sharma, S.K. Arora, Tripathi, Review of supercapacitors: Materials and devices, J. Energy Storage 21 (2019) 801–825.
[57] K.S. Ahn, R. Vinodh, B.G. Pollet, R.S. Babu, V. Ramkumar, S.C. Kim, K. Krishnakumar, H.J. Kim, A high-performance asymmetric supercapacitor consists of binder free electrode materials of bimetallic hydrogen phosphate ($MnCo(HPO_4)$) hexagonal tubes and graphene ink, Electrochim. Acta 426 (2022) 140763.
[58] R. Vinodh, R.S. Babu, S. Sambasivam, C. Gopi, S. Alzahmi, H.J. Kim, A.L.F. de Barros, I.M. Obaidat, Recent Advancements of Polyaniline/Metal Organic Framework (PANI/MOF) Composite Electrodes for Supercapacitor Applications: A Critical Review, Nanomaterials 12 (2022) 1511.
[59] V. Agarwal, P.B. Zetterlund, Strategies for reduction of graphene oxide-A comprehensive review, Chem. Eng. J. 405 (2021) 127018.
[60] A. Zandiatashbar, G.H. Lee, S.J. An, S. Lee, N. Mathew, M. Terrones, T. Hayashi, C.R. Picu, J. Hone, N. Koratkar, Effect of defects on the intrinsic strength and stiffness of graphene, Nature, Communications 5 (2014) 3186.
[61] H. Terrones, R.T. Lv, M. Terrones, M.S. Dresselhaus, The role of defects and doping in 2D graphene sheets and 1D nanoribbons, Rep. Prog. Phys. 75 (2012) 062501.
[62] Y. Jia, L.Z. Zhang, G.P. Gao, H. Chen, B. Wang, J.Z. Zhou, M.T. Soo, M. Hong, X.C. Yan, G.R. Qian, J. Zou, A.J. Du, X.D. Yao, A. Heterostructure, Coupling of Exfoliated Ni-Fe Hydroxide Nanosheet and Defective Graphene as a Bifunctional Electrocatalyst for Overall Water Splitting, Adv. Mater. 29 (2017) 1700017.
[63] D.X. Luong, K.V. Bets, W.A. Algozeeb, M.G. Stanford, C. Kittrell, W. Chen, R.V. Salvatierra, M.Q. Ren, E.A. McHugh, P.A. Advincula, Z. Wang, M. Bhatt, H. Guo, V. Mancevski, R. Shahsavari, B.I. Yakobson, J.M. Tour, Gram-scale bottom-up flash graphene synthesis, Nature 577 (2020) 647–651.
[64] Q.M. Zhang, C.Y. Wang, Z.J. Xie, Z. Zhou, Defective/doped graphene-based materials as cathodes for metal-air batteries, Energy Environ. Mater. 5 (2022) 1103–1116.
[65] A. Muzaffar, M.B. Ahamed, K. Deshmukh, J. Thirumalai, A review on recent advances in hybrid supercapacitors: Design, fabrication and applications, Renew. Sustain. Energy Rev. 101 (2019) 123–145.
[66] Q.C. Zhu, D.Y. Zhao, M.Y. Cheng, J.Q. Zhou, K.A. Owusu, L.Q. Mai, Y. Yu, A. New, View of supercapacitors: integrated supercapacitors, Adv. Energy Mater. 9 (2019) 1901081.
[67] K. Le, M.J. Gao, W. Liu, J.R. Liu, Z. Wang, F.L. Wang, V. Murugadoss, S.D. Wu, T. Ding, Z.H. Guo, MOF-derived hierarchical core-shell hollow iron-cobalt sulfides nanoarrays on Ni foam with enhanced electrochemical properties for high energy density asymmetric supercapacitors, Electrochim. Acta 323 (2019) 134826.
[68] J.B. Pang, R.G. Mendes, A. Bachmatiuk, L. Zhao, H.Q. Ta, T. Gemming, H. Liu, Z.F. Liu, M.H. Rummeli, Applications of 2D MXenes in energy conversion and storage systems, Chem. Soc. Rev. 48 (2019) 72–133.
[69] J.L. Hart, K. Hantanasirisakul, A.C. Lang, B. Anasori, D. Pinto, Y. Pivak, J.T. van Omme, S.J. May, Y. Gogotsi, M.L. Taheri, Control of MXenes' electronic properties through termination and intercalation, Nat. Commun. 10 (2019) 522.
[70] F. Pan, L.Z. Yu, Z. Xiang, Z.C. Liu, B.W. Deng, E.B. Cui, Z. Shi, X. Li, W. Lu, Improved synergistic effect for achieving ultrathin microwave absorber of 1D Co nanochains/2D carbide MXene nanocomposite, Carbon 172 (2021) 506–515.
[71] R. Kandpal, M. Shahadat, S.W. Ali, C.Z. Hu, S.Z. Ahammad, Material specific enrichment of electroactive microbes on polyaniline-supported anodes in a single chamber multi-anode assembly microbial fuel cell, Mater. Res. Bull. 157 (2023) 111983.
[72] L.J. Zhao, K. Wang, W. Wei, L.L. Wang, W. Han, High-performance flexible sensing devices based on polyaniline/MXene nanocomposites, Infomat 1 (2019) 407–416.
[73] A. VahidMohammadi, J. Moncada, H.Z. Chen, E. Kayali, J. Orangi, C.A. Carrero, M. Beidaghi, Thick and freestanding MXene/PANI pseudocapacitive electrodes with ultrahigh specific capacitance, J. Mater. Chem. A 6 (2018) 22123–22133.
[74] R. Al-Gaashani, A. Najjar, Y. Zakaria, S. Mansour, M.A. Atieh, XPS and structural studies of high quality graphene oxide and reduced graphene oxide prepared by different chemical oxidation methods, Ceram. Int. 45 (2019) 14439–14448.
[75] B. Fang, D. Chang, Z. Xu, C. Gao, A review on graphene fibers: expectations, advances, and prospects, Adv. Mater. 32 (2020) 1902664.
[76] W.W. Zhou, M.Q. Dong, Z.X. Zhou, X.H. Sun, K. Kikuchi, N. Nomura, A. Kawasaki, In situ formation of uniformly dispersed Al_4C_3 nanorods during additive manufacturing of graphene oxide/Al mixed powders, Carbon 141 (2019) 67–75.
[77] N.R. Chodankar, D.P. Dubal, Y. Kwon, D.-H. Kim, Direct growth of $FeCo_2O_4$ nanowire arrays on flexible stainless steel mesh for high-performance asymmetric supercapacitor, NPG Asia Mater. 9 (2017) e419-e419.
[78] X. He, Q. Liu, J. Liu, R. Li, H. Zhang, R. Chen, J. Wang, High-performance all-solid-state asymmetrical supercapacitors based on petal-like $NiCo_2S_4$/Polyaniline nanosheets, Chem. Eng. J. 325 (2017) 134–143.
[79] H. Tabassum, A. Mahmood, Q. Wang, W. Xia, Z. Liang, B. Qiu, R. Zhao, R. Zou, Hierarchical Cobalt Hydroxide and B/N Co-Doped Graphene Nanohybrids Derived from Metal-Organic Frameworks for High Energy Density Asymmetric Supercapacitors, Sci. Rep. 7 (2017) 43084.
[80] F. Wang, S. Sun, Y. Xu, T. Wang, R. Yu, H. Li, High performance asymmetric supercapacitor based on Cobalt Nickle Iron-layered double hydroxide/carbon nanofibres and activated carbon, Sci. Rep. 7 (2017) 4707.
[81] J. Wang, L. Zhang, X. Liu, X. Zhang, Y. Tian, X. Liu, J. Zhao, Y. Li, Assembly of flexible $CoMoO_4$@$NiMoO_4.xH_2O$ and Fe_2O_3 electrodes for solid-state asymmetric supercapacitors, Sci. Rep. 7 (2017) 41088.
[82] F. Wang, T. Wang, S. Sun, Y. Xu, R. Yu, H. Li, One-step synthesis of Nickle Iron-layered double hydroxide/reduced graphene oxide/carbon nanofibres composite as electrode materials for asymmetric supercapacitor, Sci. Rep. 8 (2018) 8908.
[83] M.A.A. Mohd Abdah, N.H.N. Azman, S. Kulandaivalu, Y. Sulaiman, Asymmetric supercapacitor of functionalised electrospun carbon fibers/poly(3,4-ethylenedioxythiophene)/manganese oxide//activated carbon with superior electrochemical performance, Sci. Rep. 9 (2019) 16782.